Volume 26
DOE/DP40200-24

LLE Review

Quarterly Report

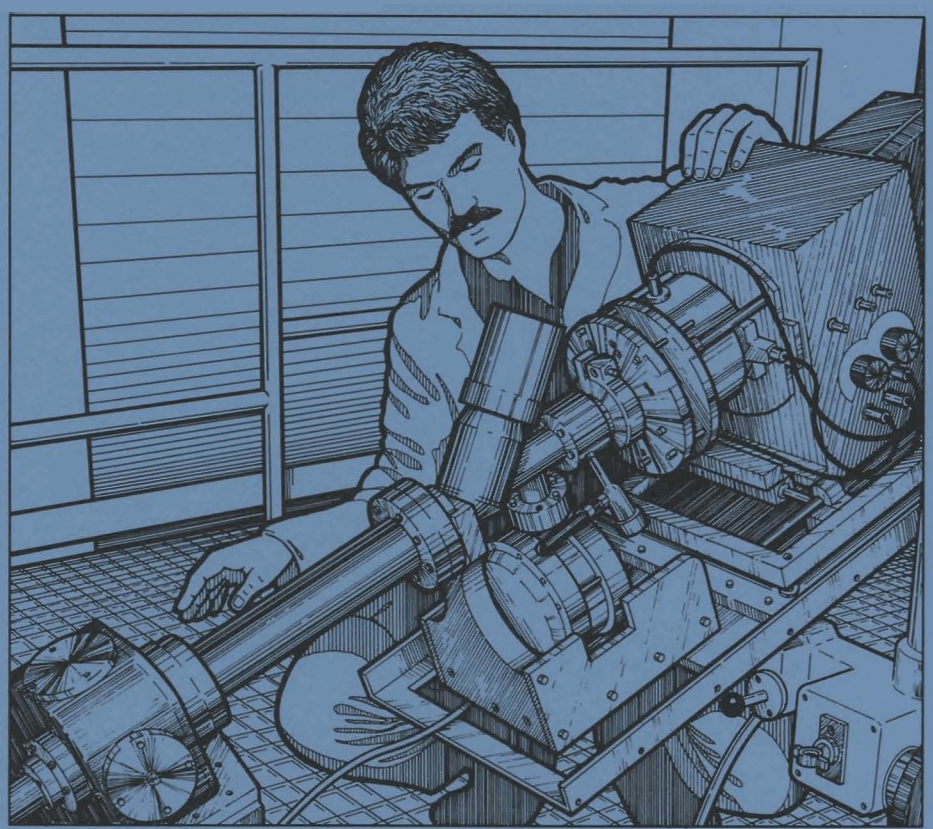

January–March 1986

Laboratory for Laser Energetics
College of Engineering and Applied Science
University of Rochester
250 East River Road
Rochester, New York 14623-1299

Volume 26
DOE/DP40200-24

LLE Review

Quarterly Report

Editor: A. Schmid
(716) 275-3541

January–March 1986

Laboratory for Laser Energetics
College of Engineering and Applied Science
University of Rochester
250 East River Road
Rochester, New York 14623-1299

IN BRIEF

This volume of the LLE Review contains reports on OMEGA and GDL laser activities; characterization of laser-generated x-ray sources for nuclear level excitation; the physics of parametric instabilities driven by two pump beams in laser-produced plasmas; developments in advanced technology areas at LLE, specifically ultra-high-speed opto-electronic devices and methods and the modeling of thin-film features in physical vapor deposition; and the National Laser Users Facility activities for January–March 1986.

The following are highlights of articles contained in this issue:

- Parametric instabilities driven by more than one laser beam are analyzed for realistic laser-driven plasmas. Growth rates and thresholds for Raman scattering by these instabilities into specific angular directions are derived and 351-nm, OMEGA experiments are called on for comparison.
- OMEGA laser-plasma x-ray yields are analyzed for their suitability in pumping novel γ-ray laser configurations. First experiments along these lines are in progress.
- A new streak spectrograph combines an x-ray streak camera with a conically curved crystal x-ray spectrograph for time-resolved spectral analysis of laser-plasma x rays. The new spectrograph has improved x-ray collection efficiency with good spectral resolving power.

- The race for the fastest device switching times among high-speed electronic circuits is accelerated by the LLE opto-electronic sampling technique, which measured a 5-ps rise time in a permeable-base transistor.
- Growth abnormalities in physically vapor-deposited optical thin films are a vexing problem for film environmental stability and high-power laser compatibility. Film growth modeling helps in eliminating the cause of these abnormalities.

CONTENTS

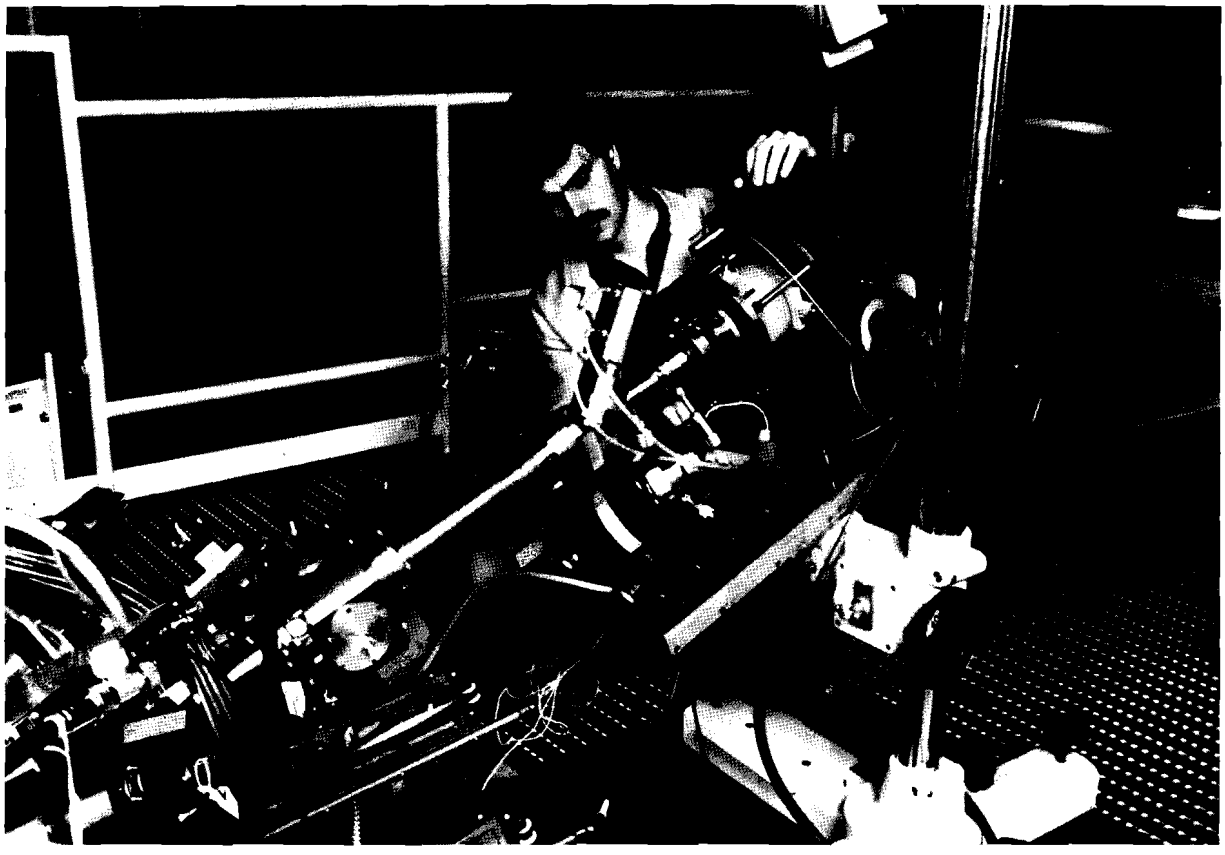

The x-ray transmission-grating streak spectrograph mounted on the OMEGA target chamber is adjusted by Robin Marjoribanks, a doctoral candidate in mechanical engineering. This instrument is used in the study of ionization in nonequilibrium plasmas.

Section 1
LASER SYSTEM REPORT

1.A GDL Facility Report

The glass development laser (GDL) facility operations during this quarter included laser-target interaction experiments, tests of several schemes to improve the OMEGA beam uniformity, and alignment and installation activity for the GDL/OMEGA integration task, which will enable GDL to provide an x-ray backlighting source for OMEGA experiments.

A summary of GDL activities during this quarter follows:

Beamline Alignment/Test Shots	149

1.B OMEGA Facility Report

During the second quarter of FY86, the OMEGA laser provided shots for a number of experimental programs and for a series of tests to determine the parameters controlling the on-target irradiation uniformity.

During this quarter the laser operated primarily in the intermediate pulse-width regime of 400 to 450 ps. Peak power generated equaled 4 TW. The experimental programs included (a) two series of National Laser Users Facility (NLUF) experiments; (b) target irradiation uniformity tests using x-ray signature targets and thin-walled DT-filled

targets; (c) x-ray streak-camera calibration and activation experiments; (d) x-ray line self-absorption spectroscopy tests; and (e) exploratory thick-walled glass target experiments.

Uniformity tests included (a) cw argon-ion laser beam tests of thermally induced beam distortion; (b) characterization of defects in crystals and other optics; and (c) tests of air-conditioning system reconfigurations to reduce the effects of microthermals on the beam uniformity.

A summary of OMEGA operations during this quarter follows:

Driver Test and Alignment Shots	208
Beamline Test and Alignment Shots	145
Target Shots	159
TOTAL	512

ACKNOWLEDGMENT

This work was supported by the U.S. Department of Energy Office of Inertial Fusion under agreement No. DE-FC08-85DP40200 and by the Laser Fusion Feasibility Project at the Laboratory for Laser Energetics, which has the following sponsors: Empire State Electric Energy Research Corporation, General Electric Company, New York State Energy Research and Development Authority, Ontario Hydro, Southern California Edison Company, and the University of Rochester. Such support does not imply endorsement of the content by any of the above parties.

Section 2
PROGRESS IN LASER FUSION

2.A Parametric Instabilities Driven by Two Pumps in Laser-Fusion Plasmas

Parametric instabilities of importance to laser-plasma interactions in laser-fusion experiments are usually analyzed assuming only one laser beam (pump) drives each instability. In actual experiments, however, multiple laser beams may overlap in a localized region of the fusion target corona, where parametric instabilities may be driven by more than one pump. In the simplest case, shown in Fig. 26.1, three-wave instabilities driven by one pump become five-wave instabilities driven by two pumps; the angle between the pumps is $2\theta_B$, the angle between the fixed positions of two illuminating beams. Five-wave parametric instabilities are the main subject of this article.

To summarize the results presented here, a homogeneous plasma model is first used to calculate growth rates and thresholds for five-wave Raman scattering and for two-plasmon decay. An inhomogeneous plasma slab with a linear density gradient is then considered. Heuristic arguments indicate that two pumps driving two-plasmon decay act independently, resulting in two inhomogeneous three-wave instabilities, instead of one five-wave process. Growth rates and thresholds for inhomogeneous five-wave Raman sidescattering are then calculated. Finally, a simple model is used to predict a spectral range of enhanced five-wave Raman sidescatter. A peak close to the one predicted is found in Raman spectra observed in six-beam, 351-nm OMEGA experiments.

Homogeneous Plasma Results

The growth rates and thresholds for five-wave parametric instabilities in a homogeneous plasma can be calculated by simple generalization

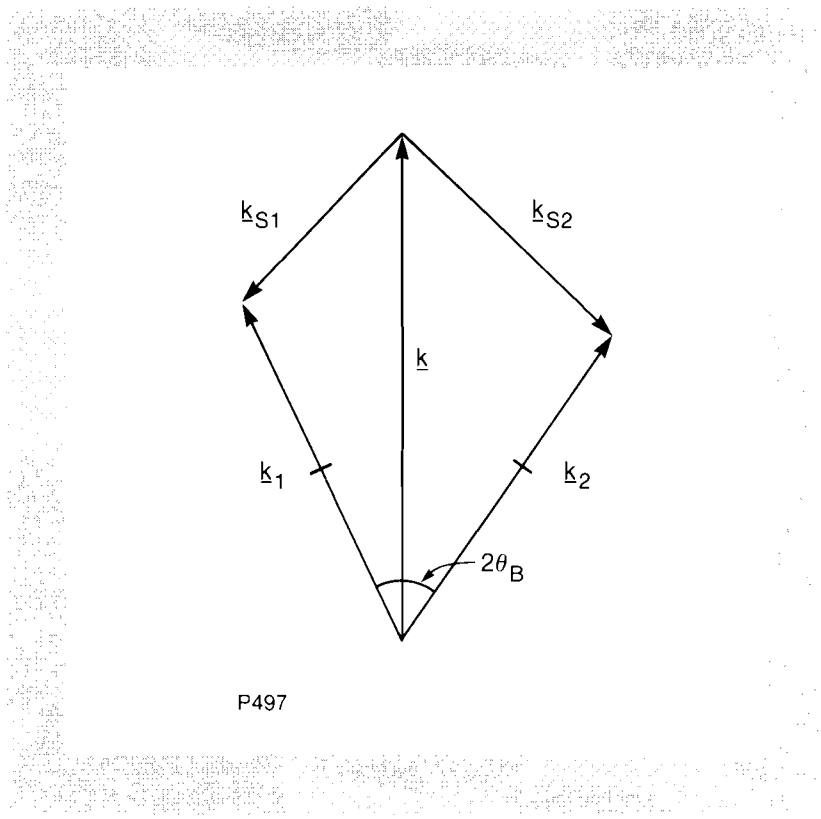

Fig. 26.1
Wave vector diagram for typical five-wave parametric instability. Two pumps $\underline{k}_1$ and $\underline{k}_2$ are at a fixed angle $2\theta_B$. The three daughter waves are $\underline{k}_\ell$, $\underline{k}_{s1}$, and $\underline{k}_{s2}$.

of the familiar calculations of three-wave instabilities.[1] The dispersion relation for five-wave Raman scattering producing two scattered electromagnetic waves, is, for example,

$$(\omega_\ell^2 - \omega_p^2 - 3k_\ell^2 v_e^2)(\omega_s^2 - \omega_p^2 - k_{s1}^2 c^2)(\omega_s^2 - \omega_p^2 - k_{s2}^2 c^2)$$

$$= k_\ell^2 \omega_p^2 [|v_1|^2 (\omega_s^2 - \omega_p^2 - k_{s2}^2 c^2) + |v_2|^2 (\omega_s^2 - \omega_p^2 - k_{s1}^2 c^2)] \quad (1)$$

Here ω_ℓ and k_ℓ are the frequency and wave vector of the longitudinal or plasma wave; ω_p is the plasma frequency; $v_e = (T_e/m_e)^{1/2}$ is the electron thermal velocity; $\omega_s = \omega_o - \omega_\ell$, where ω_o is the frequency of both pumps; k_{s1} and k_{s2} are the wave vectors of the scattered electromagnetic waves; and $|v_1| = |v_2| = |v_o|$, where $v_o \equiv (-ie E_o/m_e\omega_o)$, is the electron quiver velocity, taken to be the same for both pumps. To obtain Eq. (1), the beating of pump 1 or 2 with scattered wave 2 or 1, respectively, has been neglected. This approximation is good when, because of Bohm-Gross dispersion, the waves produced by these beat interactions do not satisfy the three-wave matching conditions; for typical experimental parameters[2] the frequency mismatch is large compared to the five-wave growth rate at perfect matching, and the approximation is well satisfied. No special coherence or phase relation between the two pumps is required to obtain Eq. (1), although each pump itself is assumed coherent. The five-wave vectors in Fig. 26.1 are assumed coplanar, with all electromagnetic wave polarizations perpendicular to their plane. This maximizes the growth rate of the instability. (If $\underline{k}_\ell$ makes an angle α with respect to the plane defined by $\underline{k}_1$ and $\underline{k}_2$, the growth rate is typically proportional to $\cos\alpha$.)

Solutions of Eq. (1) in various limits illustrate how five-wave parametric instability growth rates and thresholds differ from their three-wave counterparts. Consider Eq. (1), when one pump is perfectly matched to the plasma wave and corresponding electromagnetic wave. Write $\omega_\ell = \omega_p + \delta\omega$, and allow damping rates υ_ℓ, υ_{s1}, υ_{s2} (for collisional or Landau damping) and a frequency mismatch Δ between the second pump and second scattered wave, $\omega_o = \omega_p + (\omega_p^2 + k_{s2}^2 c^2)^{1/2} + \Delta$, and take $\delta\omega$, υ_ℓ, $\upsilon_{s1,2}$, $\Delta \ll \omega_p$. Solutions of Eq. (1) are expressed in terms of the longitudinal wave vector at perfect matching, which, neglecting Bohm-Gross dispersion, is

$$k_\ell = k_M(\omega_p, \theta) = k_o\left(\cos\theta + \left\{\cos^2\theta + \frac{\left(\frac{\omega_p}{\omega_o}\right)\left[\left(\frac{\omega_p}{\omega_o}\right) - 2\right]}{\left[1 - \left(\frac{\omega_p}{\omega_o}\right)^2\right]}\right\}^{1/2}\right), \tag{2}$$

where θ is the angle between the perfectly matched pump and k_ℓ.

Three-wave Raman results at perfect matching are recovered from Eq. (1) when $v_2 = 0$. The undamped growth rate becomes

$$\delta\omega \to i\gamma_1 \equiv \frac{i}{2} k_M |v_1| \left(\frac{\omega_p}{\omega_o - \omega_p}\right)^{1/2}, \tag{3}$$

while the threshold against damping becomes

$$\gamma_1^2 > \upsilon_\ell \upsilon_{s1}. \tag{4}$$

When $v_2 \neq 0$, the growth rate is maximized when both pumps are perfectly matched to their respective scattered waves, $\Delta = 0$. This is easily verified by treating Eq. (1) perturbatively, expanding $\delta\omega$ in integral powers of Δ. The maximum growth rate is then

$$\delta\omega \to i(\gamma_1^2 + \gamma_2^2)^{1/2} = i\sqrt{2}\gamma_1 \quad , \tag{5}$$

when $\gamma_1 = \gamma_2$. The ratio of five-wave to three-wave maximum Raman growth rates, assuming all pumps in both cases have the same intensity, is thus

$$\frac{\sqrt{2}k_M(\omega_p, \theta_B)}{k_M(\omega_p, 0)} \sim \sqrt{2}\cos\theta_B \quad ,$$

which is greater than 1 when $\theta_B < \pi/4$. In this estimate $\theta = \theta_B$ is required for perfect matching to two pumps at a fixed angle of $2\theta_B$. In the one-pump case, θ is unconstrained and Raman growth is maximized at backscattering. The five-wave Raman threshold against damping, at perfect matching, is found to be

$$\gamma_1^2 > (\upsilon_\ell \upsilon_s / 2) \tag{6}$$

for $v_s = v_{s1} = v_{s2}$. This is a factor of 2 less than the three-wave threshold in Eq. (4). When the mismatch Δ is large compared to the growth rate, the matched pump acts essentially independently of the mismatched pump.

For two-plasmon decay, the ratio of five- to three-wave maximum growth rates is just $\sqrt{2}$, independent of angle. This result corresponds to the familiar independence of angle of the maximum growth rate for three-wave two-plasmon decay.[3] Thus, one of the plasma wave vectors in the five-wave two-plasmon decay bisects the pump wave vectors, lying at the intersection of the hyperbolas of maximum growth for the three-wave decays driven by each pump.

All the homogeneous five-wave processes considered here occur in the presence of a density ripple created by the beating of the two pump waves. This ripple has been neglected in the preceding results. Calculations including the ripple show that fractional changes in growth rates are of order $(v_o/v_e)^2$, small enough to justify this approximation.

Results in a Plasma with a Linear Density Gradient

Consider now five-wave parametric instabilities driven by two pumps in a slab plasma with a linearly inhomogeneous density profile $n(x) = n_o\,(1 + x/L)$. The plasma is homogeneous in the y and z directions. For two-plasmon decay, the two-pump process appears to be suppressed under typical experimental conditions, and multiple pumps act independently, each driving three-wave decay. In the theory of inhomogeneous three-wave two-plasmon decay,[4,5] the growth rate is maximized on the hyperbola of maximum growth for the homogeneous instability. Moving off the hyperbola, the inhomogeneous growth rate falls off rapidly. Referring to Fig. 26.2, the maximum growth rate for the five-wave instability should occur when one of the three plasma daughter waves ($\underline{k}_A$) is at the intersection of the hyperbolas of maximum growth for the two pumps. Furthermore, when the parameter

$$\beta \equiv 1.41\, T_{kev}^2 / I_{14}\, \lambda_\mu^2 \gg 1$$

(where T is the electron temperature in keV, I is the pump intensity in 10^{14} W/cm^2, and λ is the pump wavelength in microns) as for OMEGA experiments with 351-nm light, the one-pump growth rate is sharply peaked near the vertex of each hyperbola. When angles between laser-beam directions are significant, as in 6-beam or 24-beam spherical configurations, the intersection of the hyperbolas is far enough from the vertices that the growth rate is much smaller than the maximum or, typically, actually negative or damped. Thus, in Fig. 26.2, the growth rate for the three-wave process including $\underline{k}_2$, $\underline{k}_p'$, and $\underline{k}_B$ is much larger than, or even has the opposite sign of, the growth rate for the three-wave process including $\underline{k}_2$, $\underline{k}_{p2}$, and $\underline{k}_A$. Since inhomogeneous two-pump thresholds and growth rates typically differ from one-pump results by factors of 2 and $\sqrt{2}$ respectively, as for the Raman results obtained next, the two-pump two-plasmon decay should be suppressed.

Modifications of five-wave Raman scattering in inhomogeneous plasmas under realistic experimental conditions are far more significant

and interesting than for two-plasmon decay. Consider Raman sidescattering with two pumps; this process[6,7] is absolutely unstable in the radial direction, and thus dominant at densities below quarter critical. Since the pumps have equal wavelengths, sidescatter constrains them to lie symmetrically about the density gradient, as shown in Fig. 26.3. In general, the longitudinal wave vector $\underline{k}_\ell$ has an arbitrary transverse component $\underline{k}_{\ell y}$. This process can be analyzed exactly as the three-wave process is in Ref. 7, where the method of analysis is explained in detail.

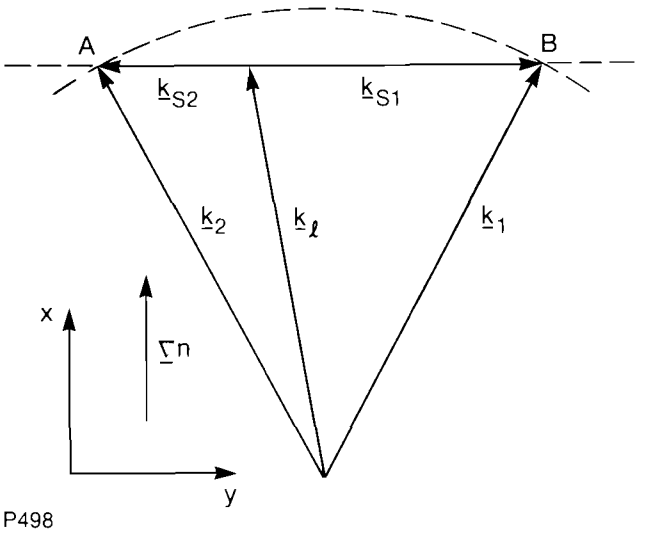

Fig. 26.2
Five-wave two-plasmon decay in inhomogeneous plasma. Three-wave growth rates are sharply peaked on the hyberbolas of maximum growth. For $\beta \equiv 1.41\ (T^2_{kev}/I_{14}\ \gamma^2_\mu) \gg 1$, *growth is further peaked near the vertices of the hyperbolas. Thus, the five-wave process, including decay wave* $\underline{k}_A$, *is weakly growing or damped when the three-wave process, including decay wave* $\underline{k}_B$, *is unstable.*

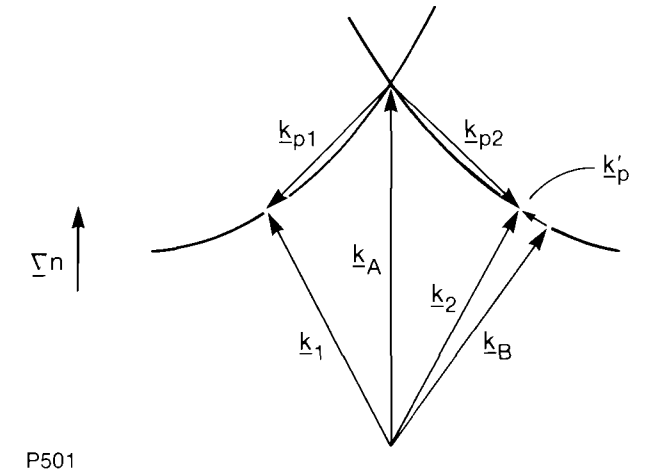

Fig. 26.3
Two-pump inhomogeneous Raman sidescattering. Pumps must lie at the intersection of the line of sidescatter along $\overline{AB}$, *and the circle* $|\underline{k}_1| = |\underline{k}_2| = |\underline{k}_o|$, *along AB.*

In the homogeneous limit this analysis yields a dispersion relation of the form $F_H = 0$, where F_H is a fourth-order polynomial in $k_{\ell y}^2$. Thus, $(\partial F_H/\partial k_{\ell y}) = 0$ at $k_{\ell y} = 0$, and the roots of $F_H = 0$ occur in pairs that are reflections of each other through the origin of the complex $k_{\ell y}$ plane, and are complex for $|k_{\ell y}| << 1$. Consequently, the instability is absolute in the y direction when $k_{\ell y} = 0$.[8] In the inhomogeneous case, it is evident from symmetry that the dispersion function D must have a double zero at $k_{\ell y} = 0$ ($\partial D/\partial k_{\ell y} = 0$ at $k_{\ell y} = 0$), and the necessary condition for absolute instability in the y direction is satisfied. Furthermore, perfect matching to both pumps requires $k_{\ell y} = 0$. For these reasons, the strongest Raman sidescattering is found when $k_{\ell y} = 0$.

In this limit, growth rates and thresholds are computed as in Ref. 7. The dispersion relation is obtained from the Bohr-Sommerfeld eigenmode condition, applied after transforming in the x direction. It is solved by perturbing about the homogeneous limit, expanding in the small parameter $(k_o L)^{-1}$. As in the homogeneous case, the growth rate with two pumps is greater than that with one pump (with the same intensity as each of the two pumps) by a factor of $\sqrt{2}$; the instability threshold for v_o^2 is lower by a factor of 2 with two pumps than with one. These results are found by making a comparison with one pump whose angle of incidence in vacuum is θ_B, and taking $k_{\ell y} = 0$ at the matching density. However, since the one-pump sidescatter process is unconstrained, growth rates and thresholds comparable to the two-pump process can be found by varying the angle of incidence, as shown by Eq. (7) and Fig. 5 of Ref. 7.

An important property of the Raman sidescattering instability considered here is that, since it can satisfy perfect matching at only one density, it is spatially localized about that density. Since each density corresponds to a unique scattered wavelength in vacuum, this localization implies a peak in scattered wavelength. The width can be estimated by taking the first pump to be perfectly matched to the first scattered wave at each radius, and by computing the mismatch for the second pump. Using the homogeneous theory discussed previously as a guide, the two pumps should act independently when the mismatch becomes larger than the sidescattering growth rate $\gamma \sim (v_o/c)\omega_{po}$. Taking $\Delta = 2\gamma$, the spectral width $\Delta\lambda_s$ can be estimated for typical parameters; $(v_o/c) \sim 10^{-2}$, $\theta_B \sim 40°$, as $(\Delta\lambda_s/\lambda_{so}) \lesssim 0.02$ where λ_{so} is the scattered wavelength at perfect matching. This estimate suggests that two-pump Raman sidescattering will produce a spectral peak corresponding to the region of matching to both pumps.

Comparison to Experiment

Since the spectrum of two-pump Raman sidescattering is so narrow in a slab model, the details of matching and spherical target-illumination geometry determine, in practice, the spectral peaks produced. The plasma frequency ω_{pM}, at which matching to both pumps occurs, is found to be

$$\left(\frac{\omega_{pM}}{\omega_o}\right) = \frac{\cos^2 \theta_v}{2} \quad , \tag{7}$$

where θ_v is the vacuum angle between each pump and the density gradient. Figure 26.4 is a schematic diagram of a spherical target

illuminated by two tangentially focused beams. Each beam is a cone converging on the sphere. For simplicity, only rays in the plane defined by the beam axes are considered. Only symmetric pairs of rays, one from each beam, contribute to two-pump Raman sidescattering. When each ray in a pair makes an angle α with its beam axis, the rays intersect at a geometric radius

$$r_G = \frac{D\, f \sin\alpha}{\sin(\theta_B - \alpha)} \quad , \tag{8}$$

where D is the target diameter, and f is the focal ratio of the lens. Refraction is neglected in obtaining Eq. (8), since, typically, $(n/n_c) \sim 10^{-1}$ at $r = r_G$ where n_c is the critical density. Note that $\theta_v = (\theta - \alpha)$ in Fig. 26.4.

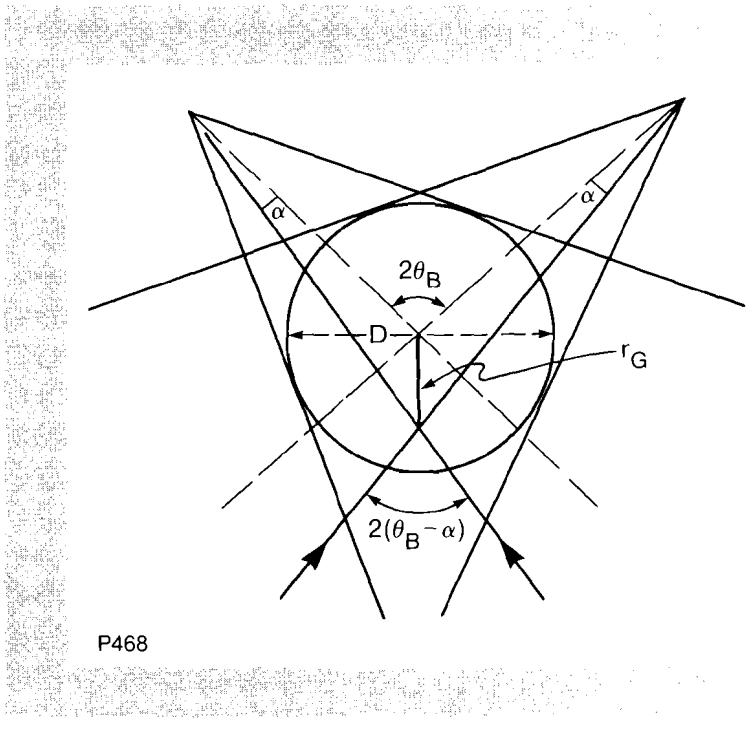

Fig. 26.4
Geometry of spherical target illuminated by two tangentially focused beams. Beam axes at angle $2\theta_B$ are shown as dashed lines. Two incident rays, shown with arrows, intersect at radius r_G.

When the density at the geometric radius r_G, given by Eq. (8), coincides with the density required by Eq. (7) to satisfy matching, enhanced Raman scattering is predicted. Moving away from the region where these densities coincide, the scattering should be suppressed because, as discussed above, the instability is sharply peaked about the matching point. The wavelength of enhanced emission is most easily found using a graphics technique, as shown in Fig. 26.5. In this figure two different kinds of curves of the scattered wavelength in vacuum, λ_s, versus radius normalized to target diameter, (r/D), are plotted. The first kind, curves A and A′, are plots of the actual density profile. The density has been expressed as the scattered wavelength $\lambda_s(r)$ that would be produced by Raman scattering at that density n(r) according to

$$\frac{\lambda_s(r)}{\lambda_o} = \frac{\omega_o}{\omega_s} = \left\{1 - \left[\frac{n(r)}{n_c}\right]^{1/2}\right\}^{-1} . \tag{9}$$

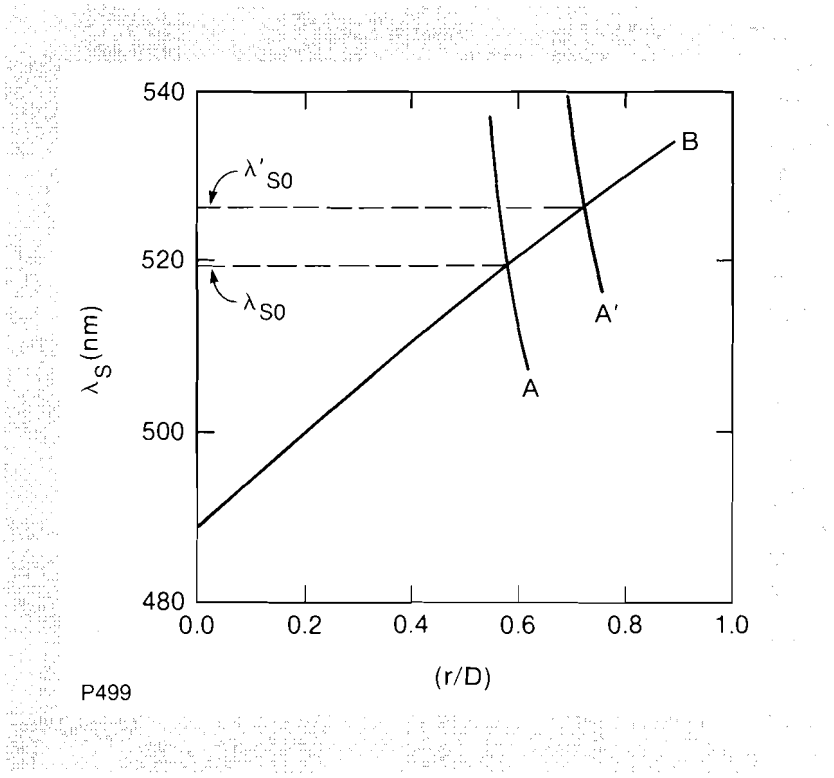

Fig. 26.5
Determination of spectral region of enhanced two-pump Raman sidescattering. Curves A and A′ are obtained from SAGE *simulations of target density profiles for parameters described in text. Curve B is obtained from Eqs. (8) and (9), with* $\theta_B = 41.3°$ *and* α *varying from 0 to* $\alpha_{MAX} = 7.13°$.

The second kind of curve, B, is a plot of $\lambda_s(r)$ corresponding, via Eq. (9), to the density required for matching at each radius n_M. Curve B is obtained by considering all possible rays in the plane of the axes of two illuminating beams of half angular width α_{MAX}. Thus, as α is varied from 0 to α_{MAX} in Eq. (8), all possible radii of intersection of pairs of rays in the beams are obtained. The corresponding density for each α is obtained from Eq. (7), with $(n_M/n_c)^{1/2} = (\omega_{pM}/\omega_o)$ and $\theta_v = (\theta_B - \alpha)$. The intersection of curves A (or A′) and B corresponds to the radius where the actual density and the density required for perfect matching are equal. Raman scattering should then be peaked at the corresponding wavelength λ_{so}. As parameters such as θ_B and α_{MAX} vary, λ_{so} will shift, and may even cease to exist if the curves no longer intersect; the latter possibility is interpreted as the suppression of five-wave Raman scattering.

Analysis of experimentally observed Raman spectra requires realistic density profiles. Such profiles have been obtained from *SAGE* simulations.[9] Since these simulations follow the target implosion in time, a time-evolving density profile n(r,t) is obtained. If the variation of n(r,t) over the width of the pulse is plotted, curves such as A and A′ in Fig. 26.5 are obtained. A corresponding spectral range of enhanced scattering, between λ_{so} and λ'_{so} in Fig. 26.5, is then predicted.

Spectra from OMEGA experiments with six 351-nm beams have been examined for the presence of two-pump Raman sidescattering, using the present model. Spectra were studied from shots with 82-μm-diameter, solid CH spherical targets, illuminated by beams tangentially focused eight target radii beyond the target center, with a pulse width of 600 ps and an average intensity of 1.8×10^{15} W/cm^2. In OMEGA

six-beam geometry the possible half angles between two adjacent beams are θ_B = 41.3° and 48.7°. Using the density profiles from *SAGE* simulations done with the same parameters as those of the experiments and a thermal flux limiter of 0.04, the curves in Fig. 26.5 are produced when θ_B = 41.3° and with α_{MAX} = 7.13°. For θ_B = 48.7°, similar curves do not intersect. Thus, a range of enhanced scattering is predicted between about 519 and 527 nm.

For comparison, two time-integrated Raman emission spectra from two different shots are overlaid in Fig. 26.6. Although the spectra differ greatly at most wavelengths, a peak between about 510 and 522 nm is seen to persist. In contrast, no such peak is evident in spectra from single beam experiments, such as those on GDL.[10] While the exact position and range of the peak differ somewhat from the values predicted by the two-pump Raman model, they are within the uncertainties of the experiment. The primary experimental uncertainty is in the pointing of the beams.[11] The axes of the beams in Fig. 26.4 can shift by as much as 20 μm within this uncertainty – which, for an 80-μm-diameter target, could (as seen from Fig. 26.5) account for 10-nm differences in the spectra. Considering, as well, the many approximations of the model, such as neglect of rays not in the plane of the beam axes, and the use of *SAGE* density profiles, the persistence of the peak provides preliminary evidence for the presence of two-pump Raman scattering.

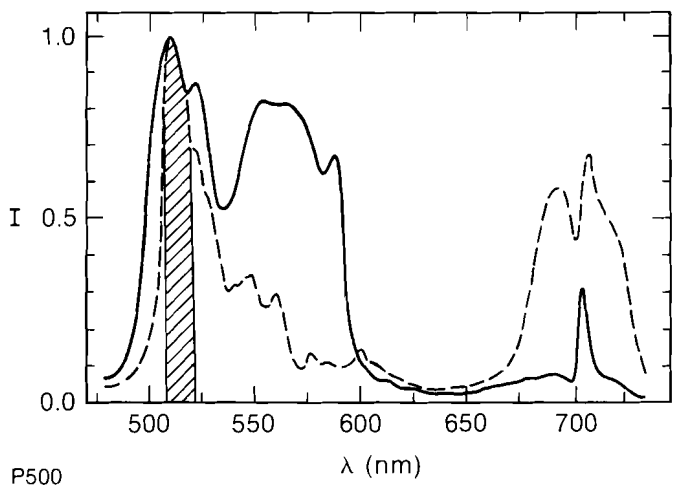

Fig. 26.6
Raman spectra from six-beam, 351-nm OMEGA experiments. Spectra from two shots made under the same conditions are superimposed. Solid CH spherical targets of diameter 82 μm, illuminated by beams tangentially focused at eight target radii, were used. Average intensity was 1.8 × 10^{15} W/cm^2 and pulse width was 600 ps. The cross-hatched region is the approximate peak common to both spectra.

Discussion

The geometrical details of the theory clearly become more complicated when Raman sidescattering is driven by more than two pumps. Qualitatively, however, it is clear that additional peaks should be present in the resulting spectra. The results for two pumps suggest that for N pumps maximum growth rates could increase by a factor of $\sqrt{N}$ and thresholds could decrease by a factor of N, compared to one pump with the same intensity as each of the N. Furthermore, the results

obtained here suggest that, in addition to the maxima associated with single-pump processes, the angular pattern of Raman scattering in multibeam experiments will have additional well-defined maxima, symmetric about the points where multiple beams symmetrically overlap. The heuristic discussion of inhomogeneous, two-pump, two-plasmon decay suggests that such additional maxima will not be found in the emission pattern associated with that process.

The results of this article imply that the interpretation of Raman spectra measured in multiple-beam direct-drive laser-fusion experiments requires a detailed understanding of Raman scattering driven by multiple pumps. Evidence indicating the occurrence of two-pump Raman scattering in blue, six-beam OMEGA experiments has been presented. Clearly, more experimental data from experiments with more beams, along with more detailed theory of multiple-pump instabilities in spherical geometry, will be required to test this interpretation.

ACKNOWLEDGMENT

This work was supported by the U.S. Department of Energy Office of Inertial Fusion under agreement No. DE-FC08-85DP40200 and by the Laser Fusion Feasibility Project at the Laboratory for Laser Energetics, which has the following sponsors: Empire State Electric Energy Research Corporation, General Electric Company, New York State Energy Research and Development Authority, Ontario Hydro, Southern California Edison Company, and the University of Rochester. Such support does not imply endorsement of the content by any of the above parties.

REFERENCES

1. J. F. Drake *et al., Phys. Fluids* **17**, 778 (1974).
2. M. C. Richardson, R. S. Craxton, J. Delettrez, R. L. Keck, R. L. McCrory, W. Seka, and J. M. Soures, *Phys. Rev. Lett.* **54**, 1656 (1985).
3. C. S. Liu and P. K. Kaw, in *Advances in Plasma Physics*, edited by A. Simon and W. Thompson (Wiley, New York, 1976), Vol. 6, p. 114.
4. C. S. Liu and M. N. Rosenbluth, *Phys. Fluids* **19**, 967 (1976).
5. A. Simon, R. W. Short, E. A. Williams, and T. Dewandre, *Phys. Fluids* **26**, 3107 (1983).
6. C. S. Liu, M. N. Rosenbluth, and R. B. White, *Phys. Fluids* 17, 1211 (1974).
7. B. B. Afeyan and E. A. Williams, *Phys. Fluids* **28**, 3397 (1985).
8. L. S. Hall and W. Heckrotte, *Phys. Rev.* **166**, 120 (1968).
9. R. S. Craxton and R. L. McCrory, Laboratory for Laser Energetics Report LLE-99 (1980).
10. K. Tanaka, L. M. Goldman, W. Seka, M. C. Richardson, J. M Soures, and E. A. Williams, *Phys. Rev. Lett.* **48**, 1179 (1982).
11. F. Marshall (private communication).

2.B Characterization of Laser-Generated X-Ray Sources for Nuclear Level Excitation

Gamma-Ray Lasers

Gamma-ray lasers have been the subject of many published proposals over the years, extensively reviewed by G. C. Baldwin *et al.*[1] More recently, the subject has received new vitality from the idea of nuclear-isomer excitation by x rays, following isomer generation by slow-neutron irradiation in a reactor.[2] The first step toward the realization of a γ-ray laser will most likely be the demonstration of nuclear isomer excitation with x-ray radiation. Such excitation depends on, and in turn contributes to, our knowledge of nuclear energy levels and their characteristics. The OMEGA laser system is capable of producing adequate x-ray flux levels for pumping certain nuclear candidates. An NLUF experiment to excite the thulium isotope ^{169}Tm on OMEGA has been proposed by C. B. Collins[3] of the University of Texas at Dallas (UTD) and is currently under way. Further experiments involving other nuclei are being planned jointly by LLE and the UTD group and are discussed here.

The principal obstacle to achieving x-ray lasing is that lifetimes of ionic levels decrease with Z (usually, as Z^{-4}). That requires the pumping power to scale as Z^6. On the other hand, nuclear-level lifetimes can be very long (up to years), when multipolarity changes by much more than 1, reducing the pumping requirements. In the past, neutron excitation was considered as a pump source for γ-ray lasers, but with discouraging results. This is mainly because neutron cross sections are small, of the order of 1 barn (10^{-24} cm^2), whereas photon cross sections are given by the Breit-Wigner formula $\sigma = (\lambda^2/2\pi)(\Gamma_r/\Gamma)$; for 1-Å radiation they typically are $10^{-19} - 10^{-17}$ cm^2. Here, Γ_r is the radiative width and Γ the total width of the upper level (this includes mostly internal conversion). This cross section for photon energy less than 100 keV can be several orders of magnitude higher than absorption losses, which in this range are mostly photoelectric (Compton scattering being small). Neutron fluxes required to cause *in situ* inversion must be unrealistically high. Also, intense bursts of neutrons are too energetic for cross sections to be sufficient, and neutron moderation is therefore necessary. The energy load on the moderator, however, will then have a destructive effect.

The lasing nuclei have to be part of a Mossbauer crystal; otherwise, the recoil energy causing shift and broadening of the γ photon will drastically reduce the stimulated emission cross section. If the crystal is perfect enough to exhibit the Borrmann effect, absorption losses in the Bragg direction will be drastically lower. Both the Mossbauer and Borrmann effects require minimum heating of the lasing medium by the bulk absorption of the pump radiation.

The procedure for the x-ray isomer pumping is as follows. First, isomeric nuclei are produced for a few months in a reactor by thermal-neutron capture in parent nuclei. Then, isotope and isomer separation produces a pure isomer sample of sufficient size – at least 1 cm^2 – to capture a sizable fraction of the x rays emitted by a laser target at a

distance of about 5 cm. The thickness of the sample has to be the e-folding distance for photoelectric x-ray absorption at the pump wavelength. Any compromise on these sample preparation requirements will reduce the signal-to-noise ratio in detecting the nuclear decay following excitation by x rays, and will necessitate gathering statistics from many laser-target shots. Ideally, pumping by x rays should transfer the isomer-level population to a very short-lived level. In this case, the broad nuclear level will intercept a wider spectral band of pump x rays. This level should then decay to the upper γ-ray laser level, for which the lifetime should be longer than the laser pulse width (~ 1 ns).

The number of excited nuclei N can be simply estimated as[3]

$$N = F_1 \times F_2 \times F_3 \times F_4 \quad , \tag{1}$$

where F_1 is the strength of the laser-irradiated x-ray source, in photons per keV per unit solid angle. F_2 is the nuclear level width (in keV) due only to the radiative transition. F_3 is the ratio of on-resonance cross section for both excitation and internal conversion, to the nonresonant (photoelectric) absorption cross section. Finally, F_4 is a correction factor that accounts for photon depletion around resonance. Only the ratio of cross sections appears because the x-ray line spectrum is continuous on the scale of the much narrower nuclear level width; thus, resonant absorption can take place away from line center, up to the point where resonant and nonresonant cross sections become equal. For the thulium experiment discussed below, $F_2 = 5.2 \times 10^{-13}$ keV, $F_3 = 560$, and $F_4 = 0.1$. Therefore, if $F_1 = 10^{14}$ keV^{-1}, the total signal is about 3×10^3 events, sufficient, when multiplied by the detector solid angle, to be observed with a small number of laser shots. This value of F_1 translates to an x-ray fluence of almost 10^{16} keV/keV into 2π solid angle (the thulium transition energy is 8.4 keV). A value of x-ray fluence above 10^{16} keV/keV is taken as a minimum for significant nuclear excitation of promising nuclear candidates. As shown below, OMEGA target shots can produce this and higher fluence levels on a single-shot basis for photon energies up to and beyond ~ 10 keV.

Proposed Nuclear Pumping Experiments

Three experiments have been designed for testing both the physical and instrumental aspects of nuclear pumping schemes. The nuclei involved are

(a) ^{169}Tm (thulium)
(b) ^{137}La (lanthanum)
(c) ^{110}Ag (silver)

The experiments will be taken up in this order, which is from least in cost to the most costly, but from the more difficult to the less difficult.

In the thulium experiment (see energy level scheme in Fig. 26.7), an excitation will be attempted from the nuclear ground level to the spin (3/2)+ level at 8.4099 keV. As an excitation source, a Cu^{+27} x-ray line from copper-coated targets was selected. The intense resonance line of this ion at 8.39 keV has been shown to be excited in OMEGA experiments (see below) with a spectral fluence of 10^{17} keV/keV. As shown above, this is sufficient to observe a signal of nuclear decay. The coin-

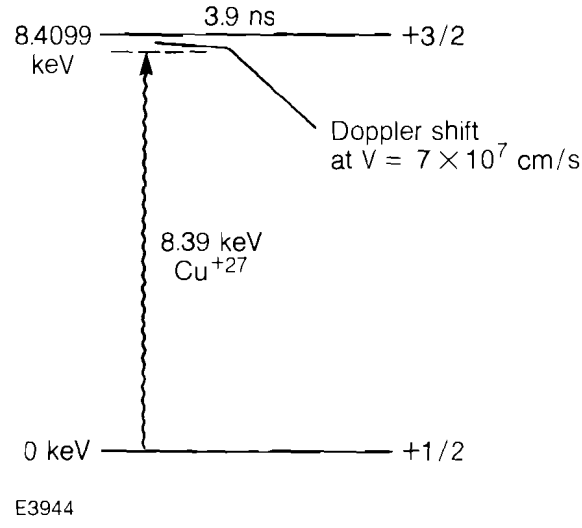

Fig. 26.7
Nuclear energy levels in ^{169}Tm. Excitation of this nuclear transition will be attempted with the 8.39-keV laser-produced x-ray line of Cu^{+27}.

cidence between atomic and nuclear transitions seems to be inexact, but the Doppler shift due to the plasma expansion from the laser-irradiated target could compensate for the energy difference.

In the geometry of the thulium experiment, the copper plasma expands toward the thulium sample, so that the Doppler energy shift would bring the two energies closer. An expansion velocity of 7×10^7 cm/s is required for perfect coincidence; this value is entirely typical of plasma expansion velocities, so an energy coincidence is almost certain. The spectrum of expansion velocities increases the probability of resonance with nuclear transitions, but the pumping efficiency is reduced because only a fraction of the radiation is useful for pumping at a given photon energy.

The signal to be measured is that of internal conversion electrons rather than the fluorescence of 8.4099-keV photons. There are two reasons for this. First, with a conversion ratio of 325, there are that many conversion electrons emitted for each fluorescence photon. Second, the fluorescence signal will not be able to compete with the scattered background radiation at the same photon energy emitted by the primary plasma. This is a major experimental problem because the plasma emission will be stronger than the nuclear fluorescence by many orders of magnitude. Thus, even the nuclear decay time's being ~ 4 times longer than the plasma emission time may prove insufficient to raise the fluorescence signal out of the background. The internal conversion electrons will be detected by a novel detector being developed for this experiment, in which thulium metal is deposited on the surfaces of a specially designed venetian-blind structure. The purpose of this design is to ensure that the short-range electrons can be extracted from the thin thulium layer and diverted by an electric field to a signal-amplifying channel-plate detector. The venetian-blind geometry prevents laser-target x rays from directly reaching the detector and thereby swamping

the signal. Finally, to take advantage of the time difference between the nuclear decay half-life (3.9 ns) and the plasma emission time (~1 ns), a gating voltage will activate the detector several nanoseconds after the laser firing, further reducing the background.

The advantages of the thulium experiment can be summarized as follows:

- 100% isotopic abundance of ^{169}Tm, so no isotope separation is needed to increase pumping efficiency.
- Pumping energy is not too high (8.4099 keV).
- Lifetime (3.9 ns) longer than laser pulse width (0.6 ns).
- High signal of conversion electrons following x-ray pumping. For a 2.5-kJ target shot on OMEGA and a detector subtending 5% of the solid angle, 6×10^4 electrons will be detected.

The second experiment, involving the ^{137}La isotope of lanthanum, is similar in conception to that of the thulium experiment. Here too we pump a ground-state nucleus to a well-known excited state, at 10.6 keV. The required photon energy is somewhat higher than that required to excite ^{169}Tm. Furthermore, we have not as yet identified an intense x-ray line that can resonate with this transition, so we will have to rely on L-shell x-ray spectra of rare-earth ions that have densely spaced line spectra in this energy range. The predicted signal strength is higher than that from the thulium experiment by about a factor of 2, in spite of the weaker x-ray pump intensity. The conversion ratio (about 1) is also more favorable. Because of this and the very long half-life of the excited state (89 ns), a measurement of the 10.6-keV fluorescence should be easy. The main difficulty is the radioactivity of the ^{137}La, which has a half-life of 60,000 years. This makes the sample more costly than the thulium sample, and the mild radioactivity requires careful shielding. In both of these experiments, a single laser shot is sufficient to yield a discernible signal. However, mapping the decay and verifying the expected half-life may require several tens of laser shots.

The third experiment, excitation of isomeric ^{110}Ag (see Fig. 26.8), is much more costly and extensive and is more characteristic of future excitation experiments of nuclear candidates for γ-ray lasers. The first difficulty is the cost of obtaining the isomeric sample. Using a sample that was not subjected to isotope or isomer separation would be the least expensive. As explained, this will necessitate the accumulation of statistics over a large number of shots. The second difficulty is that the still incomplete knowledge of the energy-level scheme renders uncertain whether a close level permits realistic pumping from the isomeric state. The 3+ level is connected by a highly forbidden transition to the 6+ isomeric state. Extrapolation of known energy-level schemes lends credence to speculation that a level with spin closer to six may lie within about 10 keV or less to the isomeric state. Covering the x-ray energy range up to about 10 keV will require several laser shots using up to ten different targets. If excitation occurs, detecting the resulting fluorescence will be relatively easy. First, the fluorescence occurs at a vastly higher photon energy than that of the x-ray pump, reducing background problems. Second, ^{110}Ag in the ground state is unstable and decays

with a convenient, 24.4-s lifetime into ^{110}Cd, providing an additional measurement of the β-decay electrons.

The successful outcome of this and similar experiments, in effect, constitutes experiments in nuclear spectroscopy: the energy and half-life of previously inaccessible levels are being determined. Such data can be used in designing optimal conditions for γ-ray lasing.

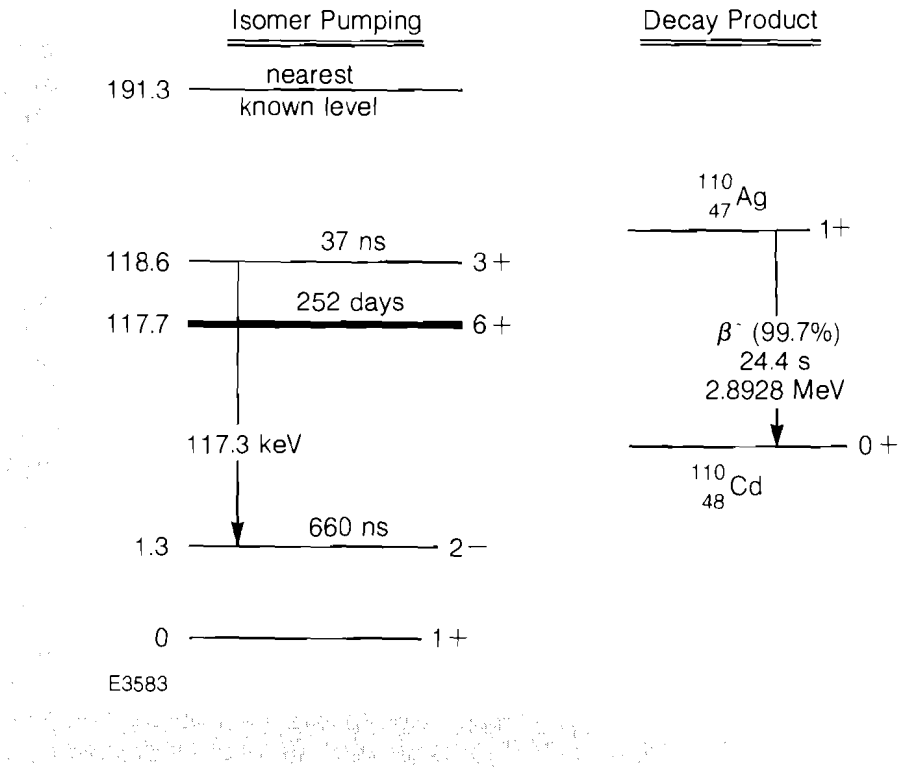

Fig. 26.8
Nuclear energy levels in ^{110}Ag. Excitation of the isomer of 252-days half-life is an example of promising nuclear pumping schemes. Once in the 1+ state, the nucleus decays via β-decay into $_{48}$Cd.

OMEGA Experiments

Experiments have begun at LLE to analyze the suitability of the x-ray pulse emitted from high-power laser-irradiated targets for exciting nuclear transitions. These experiments employed the 24-beam OMEGA laser system. For irradiating a nuclear sample with x rays from an adjacent target, 12 beams can be focused onto a flat target or a spherical target of large radius. The experiments described here were performed mostly in the former mode. In future experiments, an elongated lasing medium, where x-ray gain measurements would be attempted, is required. In this case, a multidirectional irradiation of the x-ray source in a cylindrical geometry is necessary. Such a capability has, in fact, been developed[4] on OMEGA for x-ray laser experiments.

The recent conversion of all 24 OMEGA beams into the UV (λ = 351 nm), by frequency tripling, greatly enhances x-ray production efficiency[5] and, therefore, OMEGA's usefulness for nuclear excitation experiments. In addition to high x-ray fluence, such experiments require

a wide x-ray spectral coverage to maximize the chance of resonantly exciting nuclear levels. This is essential because the location of nuclear levels is not generally well known. Thus, a continuous x-ray spectrum extending up to 10 keV could locate nuclear levels that can be pumped in a 10-keV interval extending above a ground (or an isometric) level.

The spectrum emitted by a laser-irradiated target consists of both a continuum and spectral lines. Whereas isolated spectral lines can be useful only if an occasional resonance with a nuclear transition occurs, densely spaced lines from appropriately chosen targets can serve as a quasi continuum. This adds another reason for frequency tripling, since irradiation by 351-nm light reduces preheating by long mean-free-path electrons. These electrons interact with cold material and give rise to a narrow K_α line, where the chances for coincidence with nuclear transitions are very small. On the other hand, a short-wavelength laser is coupled into a hot plasma, where the lines are broad; and a multiline spectrum, which can become a quasi-continuum, is emitted. Additionally, the virtual absence of fast electrons greatly reduces background at the energy of typical γ-fluorescence emission.

The x-ray emission from a UV-laser-irradiated target is mostly the thermal emission from a plasma in the 1-keV to 3-keV temperature range. This emission ranges up to about 10 keV in photon energy, and a laser plasma's usefulness as a source declines for much higher photon energies. On the other hand, as shown below, x-ray fluence levels as high as 10^{16} keV/keV to 10^{17} keV/keV can be achieved with a UV laser of only 1-kJ energy, over selected energy intervals below 10 keV. By choosing several target materials appropriately, one can completely cover the x-ray energy range out to 10 keV or somewhat higher energies.

The x-ray continuum (due to free-bound and free-free transitions) generally falls off with increasing photon energy, except at ionization edges. It is strongest within the sub-keV energy range because this part of the spectrum is emitted by the colder, denser target layers of the interaction region. At photon energies below about 0.5 keV, the emission is that of a blackbody. This can be seen from the formula[6] for opacity τ (absorption coefficient times length ΔR) at the ionization edge of a level of quantum number n in a hydrogenic ion of charge Z:

$$\tau = \frac{8}{3^{3/2}\,\pi^2}\;\frac{h^3\,g\,n}{m^2\,c\,e^2\,Z^2\,M_i}\;\rho\Delta R \quad . \tag{2}$$

Here, g is the Kramers-Gaunt factor, M_i is the ionic mass, ρ is the mass density, and all physical constants have their usual designations. It can be easily shown that Eq. (2) can be approximated by

$$\tau \sim 10^3\,\rho\Delta R/(TE^{1/2}) \quad , \tag{3}$$

where the relevant photon energy E and the temperature T are expressed in keV. For blackbody conditions to hold, τ should be larger than 1. For the interaction region in the target, $\rho\Delta R$ is of the order of $10^{-4} - 10^{-3}$ g/cm^2 and $T \lesssim 1$ keV, so that blackbody radiation (which peaks at $E_m \sim 3T$) occurs for photon energies less than about

0.3 keV to 0.7 keV. The radiation intensity of a blackbody can be written as

$$I \sim 10^{17} T^4 \text{ W/cm}^2 \quad , \tag{4}$$

where T is in keV. Thus, for T = 0.2 keV, the blackbody intensity (10^{14} W/cm^2) is a sizable fraction of the incident laser irradiance (typically $10^{14} - 10^{15}$ W/cm^2). High conversion efficiency (up to 50%) of the incident short-wavelength laser into sub-keV x rays has been extensively documented in the literature.[7] These high efficiencies translate to a spectral intensity in the sub-keV region of up to 10^{18} keV/keV, using a 1-kJ, short-wavelength laser. For higher photon energies, the spectral intensity as described below is considerably lower, but still substantial.

We now show results of spectra obtained on OMEGA, using either a flat-crystal x-ray spectrograph (Fig. 26.9) or a Von Hamos-type[8] focusing crystal spectrograph (Figs. 26.10–26.12). The x-ray fluence was calculated using measured crystal integrated reflectivities and published film calibration employing continuous wave x-ray sources. The uncertainty in the results due to both of these calibrations is estimated to be less than a factor of 2.

The compression of spherical targets can result in an intense x-ray continuum due to the higher density achieved at the compressed target core.[9] We show in Fig. 26.9 spectra obtained by imploding glass shell targets filled with a deuterium-tritium mixture, with and without argon, using the OMEGA laser system without the frequency tripling (λ = 1054 nm). For UV-laser irradiation (the remaining data shown here), the density in the interaction region is itself quite high ($\gtrsim 10^{22}$/cm^3), leading to high x-ray conversion efficiency even with no target implosion. However, UV-laser-driven implosion has the potential for still higher x-ray yield than that found in the experiments described below. The strong and smooth continuum is very useful for attempting the excitation of nuclear levels of poorly known location. Evidently, the continuum extends to energies above 3.5 keV; the cutoff around that energy is due to the edge of the diffracting crystal.

The continuum radiation in Fig. 26.9 is predominantly due to free-bound (recombination) transitions into Si^{+14} ions, emitted by the imploded part of the glass shell. Extending such continua to higher photon energies requires targets with higher-Z materials. This is limited by the temperature achievable at a given laser power, which has to be high enough to cause significant ionization of these higher-Z species. Experiments indicate that recombination continua of higher-Z elements up to photon energies of about 5 keV can contain significant intensity.

To extend the useful emitted x-ray spectrum to much higher photon energies, one must rely on line spectra. In general, by progressing to targets of higher-Z ions, the line spectrum changes from K- to L-, M-, and finally N-shell transitions. Here K-shell spectra mean transitions from the L-shell (n = 2) and higher shells to the K-shell, where the L-shell is mostly empty. L-shell spectra mean transitions from the M-shell and higher shells to the L-shell, where the K-shell is fully occupied and the

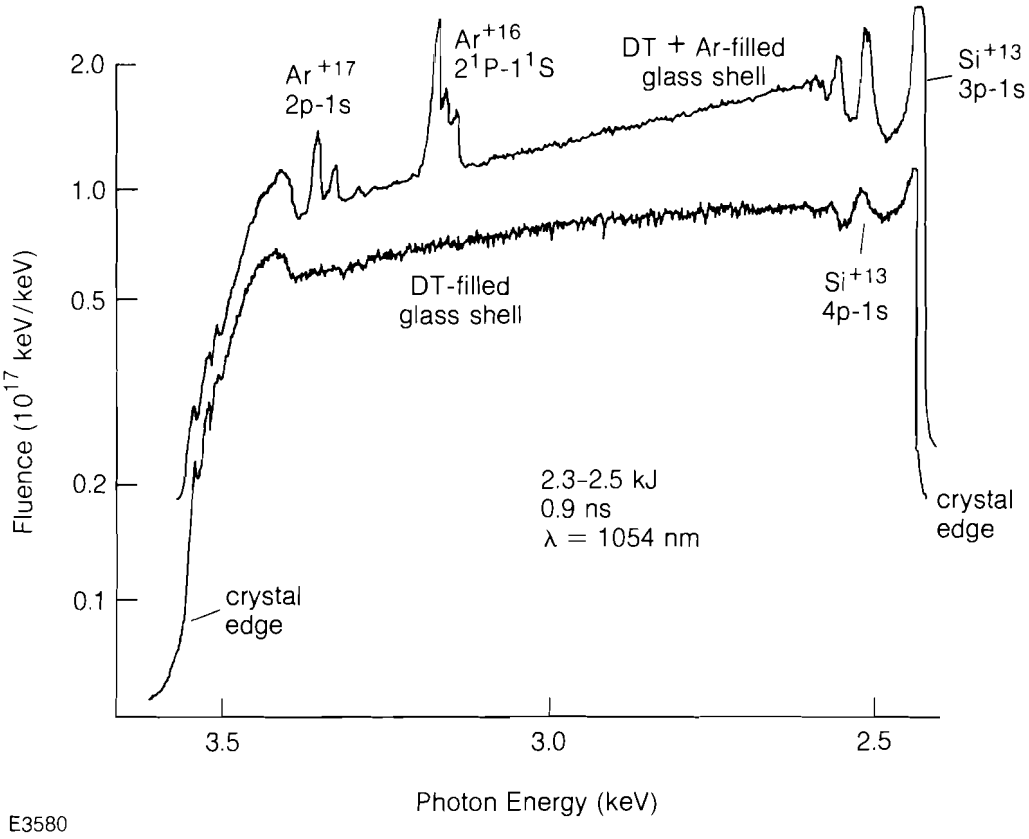

Fig. 26.9
Continuous x-ray spectra emitted from two target implosions on OMEGA. Twenty-four beams at λ = 1054 nm were used. The strong and smooth continuum is useful for attempting the excitation of nuclear levels of poorly known location.

M-shell mostly empty; thus, as one moves from K-shell to higher-shell spectra, the density of lines increases but their individual intensity, in general, declines. Therefore, for maximizing the likelihood of hitting an unknown nuclear resonance, a higher-Z target is preferable. However, a strong K-shell line is preferable when it is known to resonate with a given nuclear transition.

A case of K-shell line resonance exists between the 1^1S–2^1P line of Cu^{+27} at 8.394 keV and the transition in ^{169}Tm between the +1/2 ground level and the +3/2 level at 8.4099 keV above the ground level. This excitation is the goal of an experiment currently under way, using the OMEGA laser system to generate x rays. The line spectra in the 1-keV to 10-keV range from laser-irradiated targets of low to medium Z ($Z \lesssim 30$) are dominated by the helium-like species (e.g., Cu^{+27}), of which the 1^1S–2^1P is the strongest line.

In Fig. 26.10 we show the spectrum emitted from a copper-coated CH ball target, irradiated by the 24 OMEGA beams. The target diameter was 582 μm, overcoated with a 1-μm thickness of copper. The laser pulse, 1.46 kJ in 0.6 ns, irradiated the target symmetrically over the full solid angle, so that no more than half of the laser energy irradiated the side of the target facing the spectrometer. Each beam was focused to

a focal spot of ~50-μm diameter on the surface of the target, making the irradiance about 5×10^{15} W/cm^2. The width of the lines in these spectra is determined by the source size (since neither spectrometer focuses the radiation in the dispersion direction). The true spectral width of an individual line in Fig. 26.10, about 7 eV, is due mostly to Doppler broadening. However, the feature marked as the $1s^2$–1s2p transition of Cu^{+27} actually includes the resonance line 1^1S–2^1P, the intercombination line 1^1S–2^3P, as well as several dielectronic satellites in Cu^{+26}. A high-resolution recording of a similar spectrum (see Ref. 8b, Fig. 9) shows that a group of several lines of comparable intensity occupy an interval of about 80 eV. High resolution is achieved by irradiating a small target or using only one laser beam which is focused on the surface of the target. This is a large fraction of the width of the spectral feature at 8.4 keV, which would be ~120 eV if it corresponded entirely to spectral broadening. Part of the sloping continuum is caused by fluorescence within the spectrograph and does not represent target emission. The fluence of 1.2×10^{17} keV/keV marked for the resonance line is obtained by dividing the net intensity in the observed spectral feature by the combined estimated Doppler widths of the components comprising this feature. The uncertainty in this figure is smaller than a factor of 2.

Fig. 26.10
X-ray spectrum from a copper-coated CH ball target, irradiated by 24 OMEGA beams at λ = 351 nm. The Cu^{+27} line at 8.394 keV resonates with a transition from the 1/2 + ground nuclear level of ^{169}Tm to the 3/2 + excited state at 8.4099 keV (with Doppler shift). The x-ray fluence value for the resonance line is into 4π solid angle.

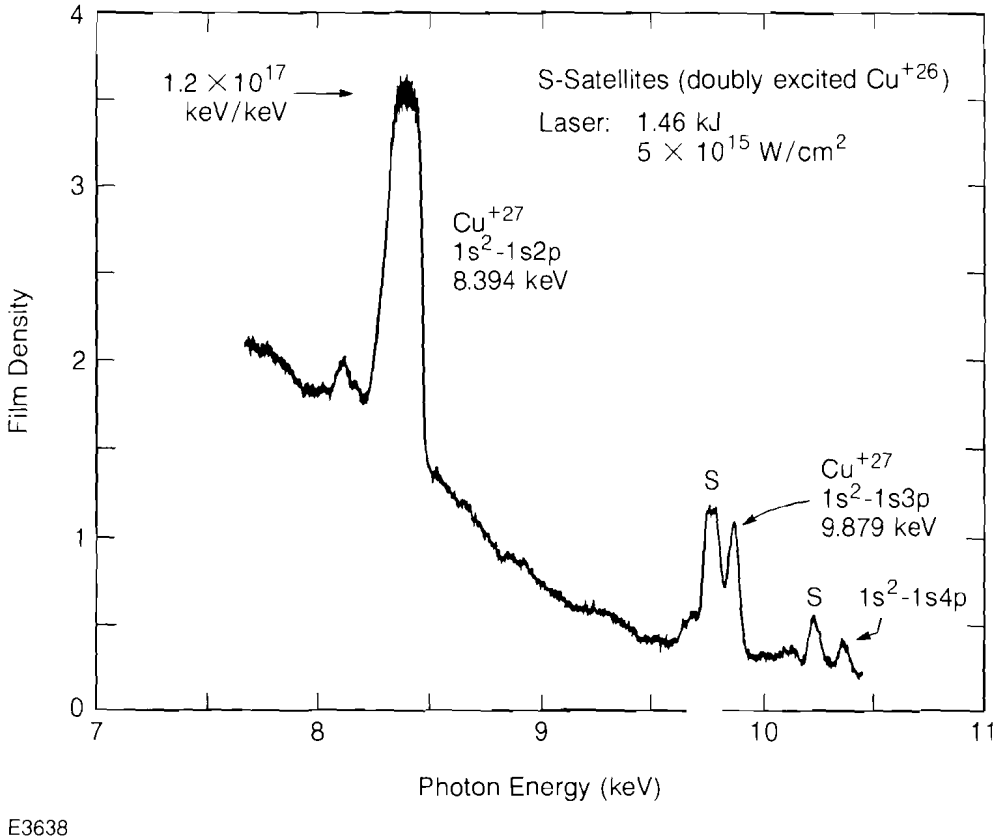

E3638

Figure 26.11 shows the spectrum obtained from a target similar to that of Fig. 26.10, after the laser energy was raised to 1.83 kJ. The resonance line here is sufficiently intense to cause film saturation (and therefore broadening). The fluence on this line is higher than 2×10^{17} keV/keV. Now not only the resonance line, but also higher energy lines, become sufficiently intense for nuclear pumping experiments.

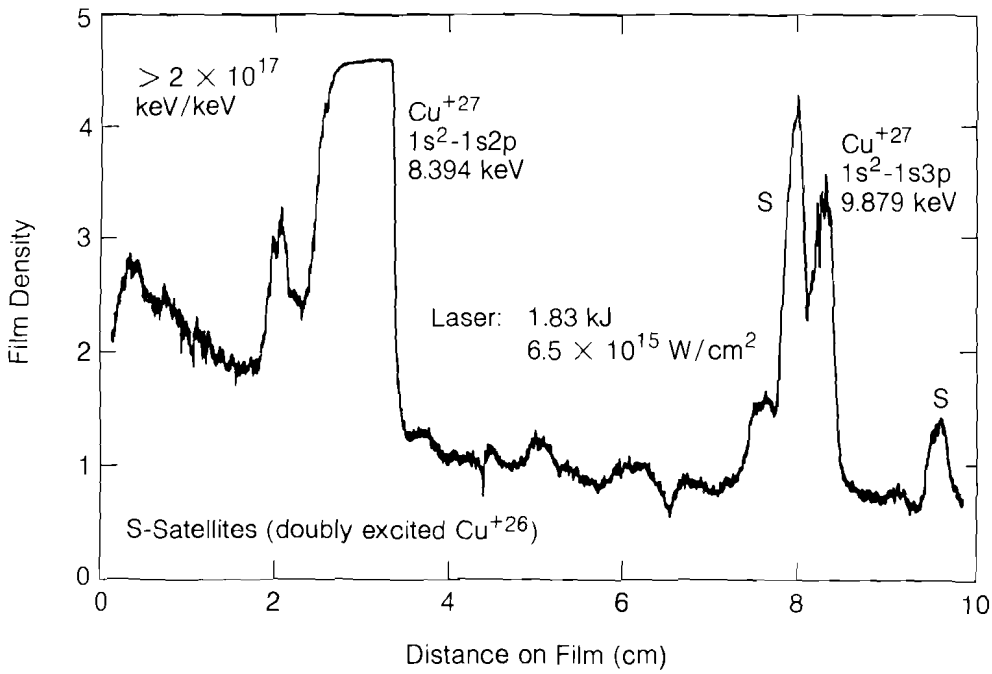

E3637

Fig. 26.11
X-ray spectrum from a similar experiment to that of Fig. 26.10, where the laser energy was raised to 1.83 kJ. The fluence within the Doppler width of the resonance line of Cu^{+27} is higher than 2×10^{17} keV/keV into 4π solid angle.

To increase the spectral coverage in the spectral range above about 5 keV (where continua are not very intense), one needs to go from K-spectra (like those of Figs. 26.10 and 26.11) to L-spectra. We have chosen a target material, praseodymium (Z = 59), whose L-spectrum falls around the 8.4-keV energy. The ionization energies of praseodymium ions with outer electrons in the L-shell range from 8.8 keV to 11.6 keV. The lines due to transitions from higher shells into the L-shell would fall roughly within the 5-keV to 11-keV range. The measured range of intense line radiation (Fig. 26.12) is about 7.6 keV to 8.6 keV. The low-energy limit is simply determined here by the edge of the diffracting crystal; the actual spectrum undoubtedly extends to lower energies. The high-energy limit is determined by the insufficiency of the plasma temperature to cause higher-energy excitations. The irradiation configuration in this experiment comprised 12 OMEGA beams; the target was moved away from the incoming beams (and the spectrograph) so that the beams converged to one focal spot of 180-μm diameter, yielding an irradiance of 6×10^{15} W/cm^2. Focusing to a smaller spot may result in a higher temperature and the extension to higher photon energies of the spectrum in Fig. 26.12. For the present

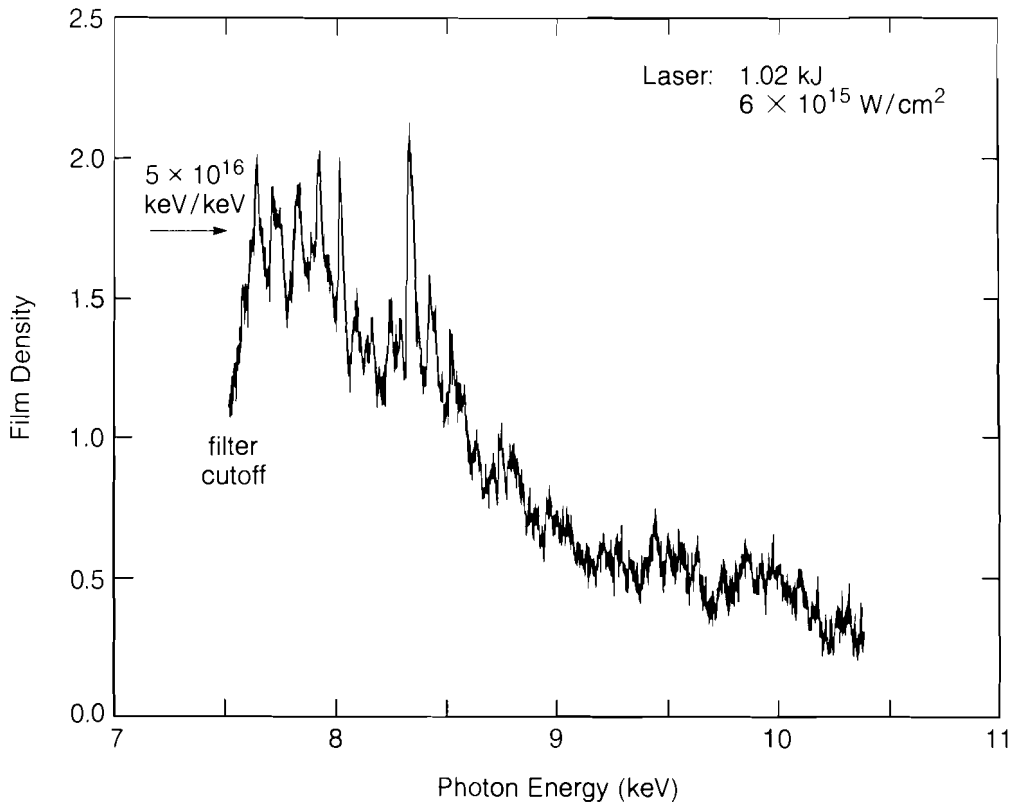

Fig. 26.12
L-shell spectrum from a praseodymium target irradiated by 12 OMEGA beams at λ = 351 nm. The 12 beams were all focused to the same focal spot of diameter 180 μm on the surface of the target.

experimental conditions we can estimate the energy interval containing the group of intense lines as extending from 6 keV to 8.5 keV. The estimated fluence of the strong lines in Fig. 26.12, 5 × 10^{16} keV/keV, is still substantial enough for significant nuclear excitation. The net coverage of the above-stated energy interval is only about 20%. This estimate is based on the true spectral widths (due mostly to the Doppler effect), which were also used to deduce the fluence estimate. If we performed experiments with rare-earth targets of successively higher Z, the spectral lines of a given type would move up in energy by about 0.3 keV for a one-step progression in Z. If the energy range covered by each target is about the same as that estimated for praseodymium (namely, 2.5 keV), a given interval in the spectrum will include spectral lines from eight successive rare-earth targets. Since the line spectrum from a single target covers about 20% of the energy range over which it extends, the cumulative effect of eight successive targets will completely cover that range. Complete coverage with fluence higher than 10^{16} keV/keV, using this procedure, is expected to apply to at least the 5-keV to 10-keV energy range. Higher energies will be accessible if higher temperatures than those achieved here can be achieved, e.g., by tighter focusing.

In conclusion, experiments on the OMEGA laser system can produce x-ray fluences of at least 10^{16} keV/keV, or about 1 J/keV, in one shot, for photon energies of up to about 10 keV. X-ray fluences of this order of magnitude are surmised to be sufficient to induce nuclear excitation in several nuclei, either in the ground state or in an isomeric state, to an extent permitting reliable measurement of the resulting nuclear fluorescence (gamma photons or internal conversion electrons). However, the radiation has to cover an energy range that includes the energy of the nuclear transition to be pumped. We showed that in the range up to about 10 keV OMEGA can achieve this condition with either one target or a sequence of up to ten different targets. Further work on optimizing the production of x rays by changing the laser and target parameters could possibly increase the x-ray fluence and extend it to above 10 keV.

ACKNOWLEDGMENT

This work was supported by the U.S. Department of Energy Office of Inertial Fusion under agreement No. DE-FC08-85DP40200 and by the Laser Fusion Feasibility Project at the Laboratory for Laser Energetics, which has the following sponsors: Empire State Electric Energy Research Corporation, General Electric Company, New York State Energy Research and Development Authority, Ontario Hydro, Southern California Edison Company, and the University of Rochester. Such support does not imply endorsement of the content by any of the above parties.

The work by the University of Texas is funded under a National Laser Users Facility contract funded by the U.S. Department of Energy.

REFERENCES

1. G. C. Baldwin, J. C. Solem, and V. I. Goldanskii, *Rev. Mod. Phys.* **53**, 687 (1981).
2. C. B. Collins *et al., J. Appl. Phys.* **53**, 4645 (1982).
3. C. B. Collins, Proposal No. 101 to the National Laser Users Facility at the Laboratory for Laser Energetics (1985).
4. LLE Review **21**, 27 (1984).
5. B. Yaakobi, T. Boehly, P. Bourke, Y. Conturie, R. S. Craxton, J. Delettrez, J. M. Forsyth, R. D. Frankel, L. M. Goldman, R. L. McCrory, M. C. Richardson, W. Seka, D. Shvarts, and J. M. Soures, *Opt. Commun.* **39**, 175 (1981).
6. C. W. Allen, *Astrophysical Quantities* (Athlone Press, London, 1973), p. 96.
7. See, for example: W. C. Mead *et al., Phys. Rev. Lett.* **47**, 1289 (1981); LLE Review **22**, 60 (1985).
8. B. Yaakobi, R. E. Turner, H. W. Schnopper, and P. O. Taylor, *Rev. Sci. Instrum.* **50**, 1609 (1979); B. Yaakobi and A. J. Burek, *IEEE J. Quantum Electron.* **QE-19**, 1841 (1983).
9. B. Yaakobi, H. Deckman, P. Bourke, S. Letzring, and J. M. Soures, *Appl. Phys. Lett.* **37**, 767 (1980).

2.C A Time-Resolving, Conically Curved Crystal Spectrograph for Laser-Plasma Studies

Analysis of x-ray line emission has long been used in measuring temperature and density in high-temperature plasmas, both astrophysical and laboratory produced. The emission lines produced, their precise wavelengths and spectral shape, and their relative intensities all provide information on detailed plasma conditions.[1] For laser-produced plasmas, the plasma conditions strongly reflect processes of absorption of laser energy, heat, and compression of the material: x-ray analysis helps elucidate the physics of each process. Among laboratory plasmas, laser-produced plasmas stand out in their ultrashort (nanosecond to picosecond) time behavior and in the extremes of high densities and temperatures produced. These conditions make laser plasmas important tools for extending our theoretical understanding and modeling of transient ionizations and atomic-state physics.[2] Such studies are of particular value to current investigations of x-ray laser schemes.[3]

To pursue these issues with laser plasmas requires spectrographs capable of providing good time resolution (< 50 ps) with at least moderate spectral resolving power ($\lambda/\Delta\lambda \gtrsim 500$). Currently, the combination of a Bragg crystal spectrograph and an x-ray streak camera, recording an x-ray spectrum dispersed in time,[4] is the best answer to these needs. Such devices are capable of less than 20-ps time resolution, and spectral resolving power $\lambda/\Delta\lambda$ greater than 1000.

In addition to good temporal and spectral resolution, the design of some experiments requires large quantum collection and efficiency. An example of such a need is in studies in which thin layers or small amounts of specific materials are embedded in the shell or fuel to provide an x-ray emission signature at some stage in the interaction process. In such studies, the perturbation induced by the signature material on its host should be minimized, and so the amount of material, and its emitted radiation, is designed to be minimal. The detection of weak x-ray signals, with high time and spectral resolution, poses special problems in laser-fusion experiments. One approach to increasing collection efficiency has been to locate the camera closer to the plasma. Given the steadily increasing energy of multikilojoule laser systems used in fusion-related studies, and the hostile magnetic and plasma environment near a target, there is much interest in changes that permit streak spectrographs to be located further from the target, while still more efficiently recording the x-ray emission.

Image intensifiers exposing photographic film already have efficiencies adequate to record single electrons incident on the phosphor of the streak camera's image converter tube, and so the objective must be to increase the photoelectron signal. One avenue has been the search for different photocathode materials of higher x-ray quantum-conversion efficiency.[5] Another approach has been to change the design of the image converter tube through the introduction of an electron-optic astigmatism that permits the use of a wider streak slit by condensing the width of the slit to a line, while still imaging along the slit length;[6] in this

way, the slit subtends a large solid angle without compromising the time-resolution contribution determined by the ultimate width of the streak slit imaged at the phosphor.[7] Third has been the development of spectrographs of moderate resolution that intercept and focus a greater solid angle of radiation.

The most notable of such collecting crystal spectrographs is the Von Hamos cylindrical spectrograph.[8] In this design, a curved crystal defines a cylinder whose axis passes through the radiation source point. Owing to the cylindrical symmetry, all rays of a given wavelength emanating from the source point reconverge on this same axis (where photographic film is positioned) after Bragg reflection at the cylindrical crystal. For an extended source, most points lie some small distance from the cylinder axis, resulting in imperfect convergence; in practice, focused intensities 100 times those of planar crystal spectrographs are reached.[9,10]

This spectrograph design is somewhat inconvenient for use in conjunction with x-ray streak cameras, since the spectral focus is along a radial axis, whereas image converter tubes are most conveniently and commonly used with photocathodes normal to this axis. The use of a Von Hamos spectrograph with a streak camera in this orientation results in effective collection of only a very narrow spectral range in the region near the intersection of the Von Hamos and photocathode axes,[11] since the Von Hamos focusing degrades quickly for points removed from its axis. In the true Von Hamos configuration, the need to orient the image converter tube perpendicular to a radius from the target generally requires that the streak camera be situated completely outside the principal vacuum chamber.[12] For laser-fusion target chambers this added distance, and the fixed Von Hamos geometry, typically results in awkwardly large dispersions.

Designs permitting spectra to be focused in a line perpendicular to the radius from the target include crystals bent to the figure of a section of a cone,[13] and to the figure of a section of a torus.[14] The latter configuration demonstrates 50 times the brightness of a comparably deployed flat crystal, while imaging the target at the same time. Here we describe the experimental implementation of a conically bent crystal spectrograph originally described by T. A. Hall,[13] using a Muscovite mica crystal bent to a cone figure of 23.1° half-angle. The spectrograph, when coupled to an x-ray streak camera, time-resolves He-like lines and Li-like satellites useful in determining the density and temperature of thin layers (0.05 μm–0.1 μm) of Al and Ti, isolated in spherical CH targets, during irradiation by the 24-beam, 351-nm OMEGA laser system. Examples of the data produced by a preliminary version of the spectrograph are drawn from some of these experiments.

The conical-crystal spectrometer has been proposed[13] as a modification of the Von Hamos design [Fig. 26.13(a)] for focusing a spectrum along a line perpendicular to the radius from the target, rather than along it. This is accomplished by curving the spectrometer crystal to a section of the surface of a cone oriented as shown in Fig. 26.13(b). In this configuration, the cone has its apex lying in the recording plane

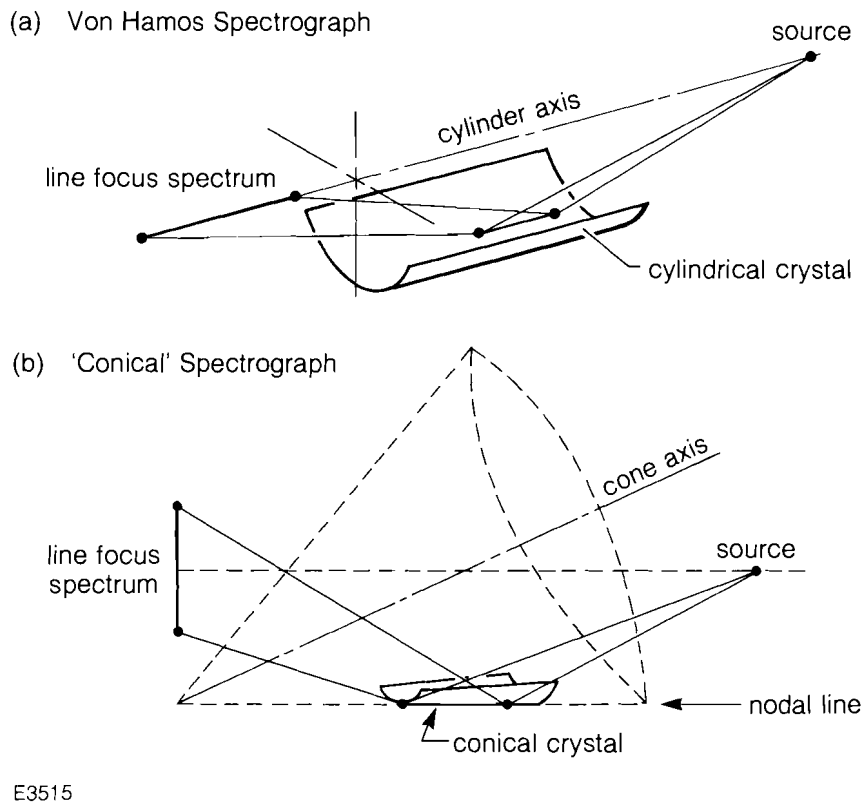

Fig. 26.13
Comparison of (a) Von Hamos and (b) conical x-ray-collecting crystal spectrograph designs. The conically bent crystal spectrograph produces a spectrum focused in a line perpendicular to the line of sight to target.

(lying perpendicular to a radius from the source), its cone axis crossing this radius at the midpoint, and its nodal line parallel to the radius. This crystal curving is a simple sheet bending (bent in one direction only) and is suitable for a wide range of crystals and radii.

In projecting the spectrum into a line perpendicular to the radius axis, two advantages of the Von Hamos design are necessarily lost. In the Von Hamos geometry, source and image are nominally equidistant from the point of reflection at the crystal. As a result of this symmetry, the spread of wavelengths due to the mosaic structure of the crystal survives only in second order (mosaic focusing).[10,15] Consequently, mosaic crystals, which generally have high integrated reflectivity, can be used without disadvantage in resolution. For spectrographs that form a perpendicular spectrum, this symmetry and the benefits of mosaic focusing are lost,[16] except perhaps for a very small region of the image near the source radius.

For the ideal case of a single-point source, the focusing of an ideal Von Hamos spectrograph is perfect, and all rays of a given wavelength obviously take the same transit time to their image point, a concern to time-resolving applications. That ideal case is impossible to recreate in a perpendicular-spectrum spectrograph; even a single-point source

cannot be made to image perfectly with all rays arriving simultaneously.[17] The conical spectrograph, and others like it, therefore depend on detailed analysis, usually ray tracing, to evaluate their temporal, spatial, and spectral characteristics.

With such ray tracing for a conical spectrograph, Hall[13] has shown quantitatively that, as the width of the cone surface used increases, the size of a point source's aberrated image increases in the imaging direction, i.e., perpendicular to the line focus. Along the spectral axis, the image size increases more slowly with increasing crystal width, and then decreases to an optimal value before again increasing monotonically. Hall also calculated the resolving power that results from this spectral confusion, convolved with the intrinsic limits of the crystal, and derived its dependence on wavelength about the best-imaged point. Using a 45° cone angle, and 0.02 as the ratio of (crystal width)/(image-plane distance), he found that for a roughly $\pm 10\%$ wavelength range about the optimal wavelength the resolution of the spectrograph is limited by the crystal, rather than the geometry.[18] Also, he calculated the focused intensity of the spectral image; over a large range of incident Bragg angles, this calculated brightness is more than 1000 times the brightness obtained from a planar spectrograph of similar specifications.

In combination with an x-ray streak camera, the brightness improvement is somewhat less than this figure. Once the image of the source lies completely within the limits of the streak camera slit aperture, there is no further gain in brightness in the streaked image as spectrograph focus is improved. Instead, for conventional electron-optic designs in which the slit aperture is imaged across its width, the streak slit image at the phosphor is narrowed, and the contribution of the writing speed and slit width to the overall time-resolution limit is reduced. In the device described here, a 1-mm slit width is used at the photocathode to facilitate alignment of the spectrograph. The width of the line focus, imaged at the phosphor, thus determines the writing-rate time-resolution limit.

Implementation

Crystal support mounts for the LLE spectrograph were fabricated on a conventional precision lathe, turning a frustum of a hollow cone of 23.1° cone half angle (Fig. 26.14). The narrow end of the frustum had an inside diameter of 19.25 cm, the base, one of 26.80 cm. The inner surface of the frustum was figured as the crystal-bearing surface and was machined to about $\pm$ 25-μm tolerance with slow variation over a scale of about 5 mm. On a smaller scale, the surface roughness was absorbed in gluing the crystal. Before the piece was removed from the lathe, a series of scores was cut, by a tool bit, into the outside surface of the frustum to provide an accurate alignment reference of the cone's nodal lines. Later, the piece was sectioned into a number of mounts 3.8 cm $\times$ 9.5 cm by cutting along every other scored line. The mounts were aligned in a jig, using the nodal lines, to affix attachment rings.

Mica (Muscovite) crystals were mounted on these substrates. They had been designed so that the Bragg condition ($n\lambda = 2d \sin\theta$) would be satisfied for He-like resonance emission ($1s^2$–$1s2p$: $^1S_0$–$^1P_1$) from Al

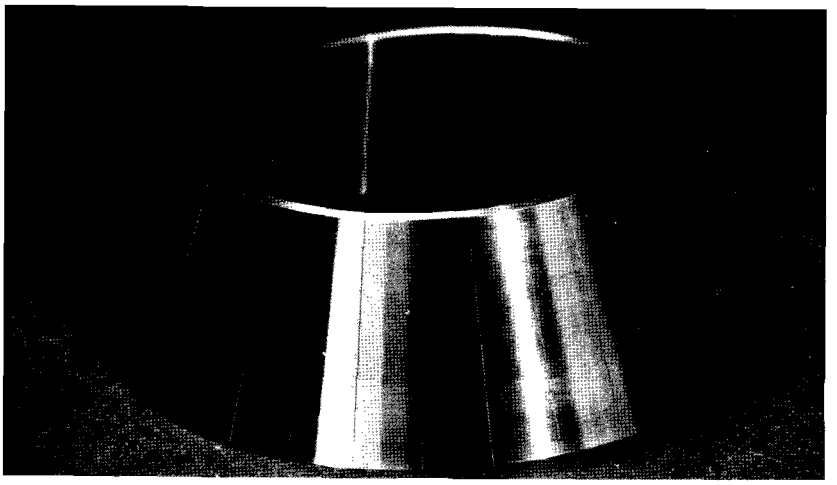

E3968

Fig. 26.14
Photograph of section of a cone, lathe-turned in aluminum, from which several mounts for spectrograph crystals were cut.

(λ = 7.757 Å; in first order) and Ti (λ = 2.62 Å; in third order) near the optimum point of the crystal midway between source and photocathode. The overall wavelength range dispersed at the photocathode was 7.5 Å < n λ < 8.1 Å in nth-order Bragg diffraction. Two different crystal attachments were investigated: vacuum mounting, using a low-viscosity cyanoacrylate glue to hold the crystal permanently, after it was drawn down onto the mount by evacuating through several tiny holes in the substrate; and pressing the crystal into a layer of epoxy.

The mounted crystal was attached to the streak camera as shown in Fig. 26.15. Critical to the spectrograph setup is the precise positioning of the apex of the spectrograph cone in the plane of the photocathode,

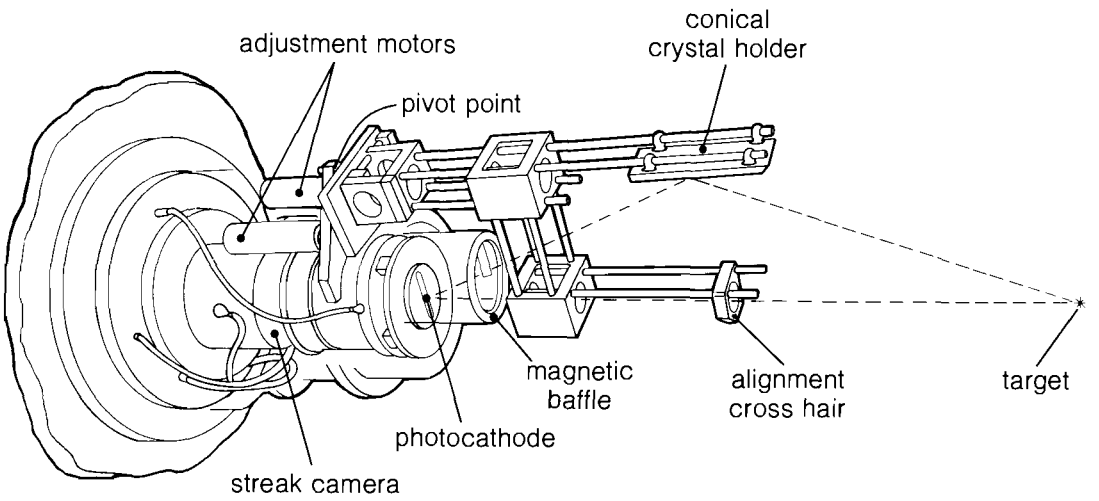

E3409

Fig. 26.15
Configuration of the conical streak spectrometer. The crystal holder is positioned in its mount in such a way that the apex of the cone to which it belongs coincides with the pivot point of the mount. Remotely controlled adjustment motors then align the crystal to the target.

along the axis of the photocathode slit. This is accomplished by supporting the crystal mount on a frame that pivots on a spherical bearing centered on that position. Then the crystal mount is set in the frame, with the nodal line passing through that point. Part of this frame rests on two linear actuators oriented 90° apart relative to the pivot. This permits the spectrograph to be aligned to the target remotely in vacuum, while remaining aligned to the streak camera.

To align to the target, a cross hair was mounted above the spectrograph at the same distance calculated for the height of the photocathode center above the cone apex. In use, then, a telescope installed opposite the device was aligned to the axis between target and the center of the photocathode, and the structure was remotely driven to place the cross hair on this axis. This procedure ensured that the spectrograph was oriented with its cone nodal line parallel to the target-photocathode axis, and at the correct distance. In use, there was little difficulty in aligning the spectrograph to the 1-mm streak slit.

The streak spectrograph was a modified RCA 73435 design,[19] deployed re-entrant to the target chamber and evacuated along with it to a pressure of 5×10^{-6} Torr. The target-to-photocathode distance was 57 cm, producing a dispersion of about 19 mÅ/mm at the photocathode. The streak camera itself was capable of a spatial resolution of roughly 10 ℓp/mm, and overmatched the spectral resolution expected for the spectrograph. This overmatching was to improve quantitative data reduction, particularly that of line shapes.

Experimental Results

The conical streak spectrograph was used in recording x-ray emission from targets irradiated with the OMEGA 24-beam UV (351-nm) laser system. Parylene (CH)-coated spherical targets were used in which a spherical, 0.05-μm- to 0.1-μm-thick layer of Ti or Al was located at a depth of 1.5 μm–2.5 μm (Fig. 26.16). In addition, data were taken for

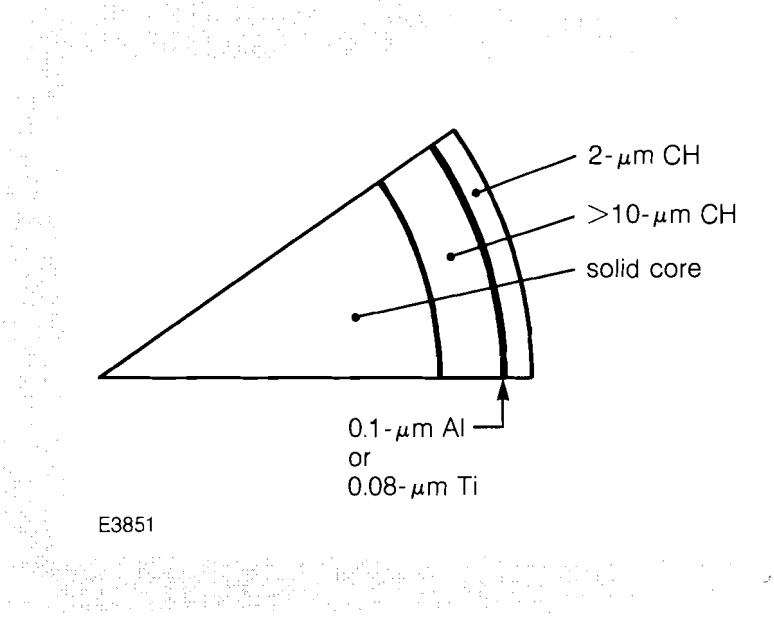

Fig. 26.16
Schematic drawing of the thin-layer targets used. Thin layers of aluminum or titanium were located within plastic targets, to produce x-ray emission characteristic of plasma conditions at that depth.

several DT-filled microballoons to which Kr had been added as a diagnostic emitter. All targets were uniformly irradiated at a peak intensity of 4×10^{14} W/cm^2, and He-like spectra as well as Li-like satellites of the metallic layers, or emission from Si and Kr, were time resolved.

A comparison of spectra, taken with the streak spectrograph, of thick (2-μm) and thin (0.1-μm) Al layers is shown in Fig. 26.17. For this figure the film response characteristics are already removed, but no account of the reflectivity of the mica for different wavelengths is taken. Mica shows strong features in its spectral reflectivity over this range. In this case, the thick Al was bare, and the thin layer was buried at a depth of about 2 μm. Without additional attenuation, the intensity from the thicker Al layer was excessive and, during the streak, produced severe photoelectron-current pinching in the imperfect vacuum of the tube.

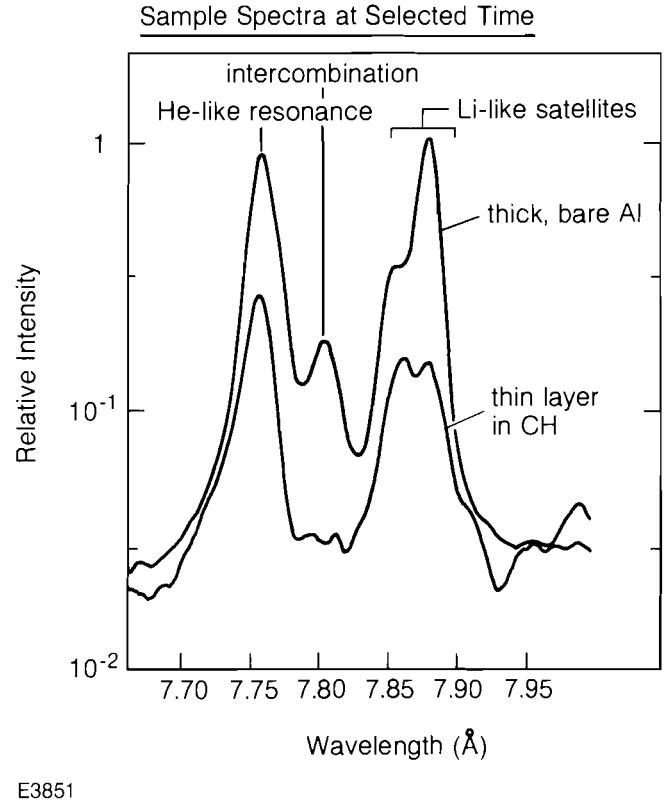

Fig. 26.17
Comparison of spectra taken at early time in the emission from a thick (2-μm) bare aluminum target, and from a thin-layer target of the type in Fig. 26.16. The times at which each spectrum was taken are not the same with respect to the laser pulse.

Similar spectra from a thin, embedded Ti layer are displayed in Fig. 26.18(a). Time traces made of each line feature can be seen in Fig. 26.18(b). Ratios of these lines help in determining the temperature and density[20] evolution of the emitting region, which, for sufficiently thin layers, is well localized.

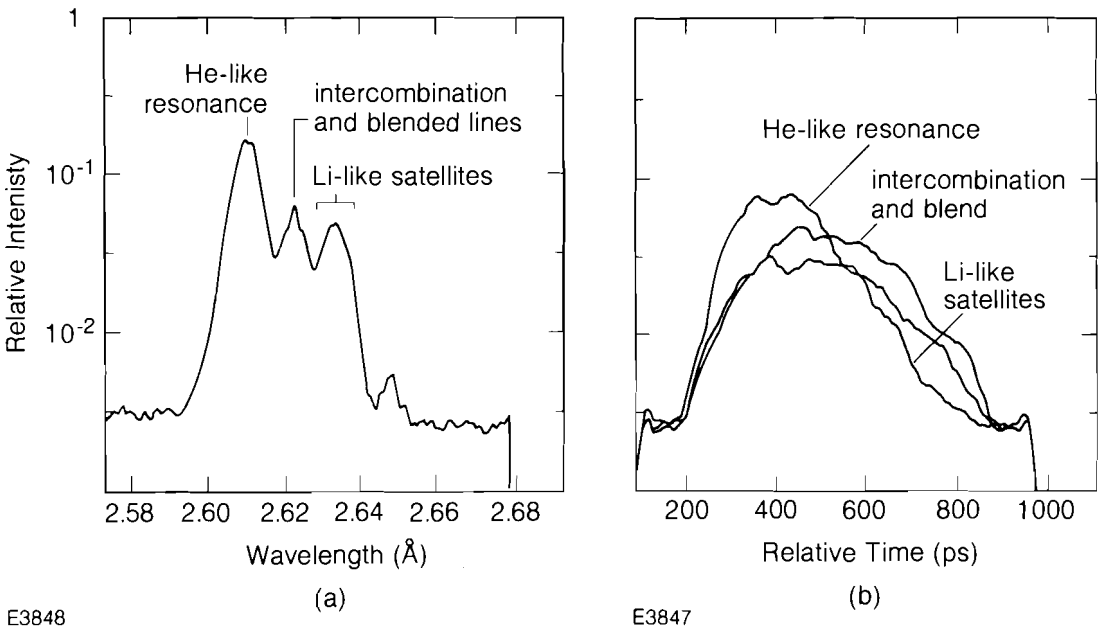

Fig. 26.18
Sample spectrum (a), produced at a selected time, from a titanium thin-layer target of the type shown in Fig. 26.16. Part (b) shows the history of emission of several spectral features during the laser pulse.

Figure 26.19(a) shows a perspective plot of the emission dynamics during the implosion of a Kr/DT-filled glass microballoon. A sample spectrum at a selected time is shown in Fig. 26.19(b).

Conclusions

The streak spectrometer produced by combining a conically bent crystal spectrograph with an x-ray streak camera provided an effective device for time-resolving low-flux spectra from laser-produced plasmas. The intensity improvement over a similarly deployed planar-crystal spectrograph should be equal to the ratio of widths at the crystal that subtend the streak slit; this indicates a collected-flux increase of a factor of 50–100, consistent with observation.

The time resolution of the current system is limited by the effective width of the streak-slit image at the phosphor and is estimated at 40 ps. With characterization of a better-focused spectrum, or with an astigmatic electron-optic design, this figure can be lowered to 10–20 ps. The spectral resolving power of the time-resolving system is estimated at $\lambda/\Delta\lambda \sim 600$, currently limited by the quality of the figure of the crystal mount. This is highlighted by data taken with crystals that had been vacuum mounted: vacuum mounting produced excellent conformation to the substrate, and in data taken with such mounts, very small periodic machining irregularities produced substantial structure in the spectra.

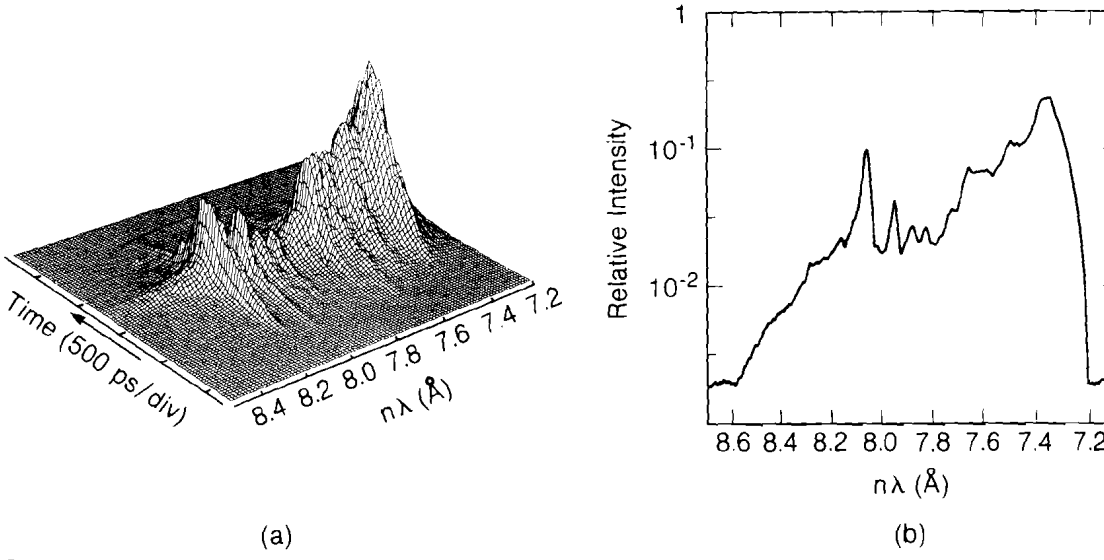

Fig. 26.19
Perspective plot (a) of the temporally and spectrally resolved emission from an imploding deuterium- and tritium-filled microballoon target, to which a small amount of krypton gas was added. A sample spectrum, taken at a time near the peak of emission, is shown in (b).

Recently, high-quality diamond-turned mounts have been prepared. Mica, used in third order, has been retained for studies of Ti He-like resonance, and, in second order, for Ar-filled microballoon implosions. The large degree of structure in the first-order spectral reflectivity of mica in the region of interest makes it inappropriate for studying Al emission around 7.8 Å. Mica has been replaced by KAP mounted on a 17.05° half-angle cone. With these changes implemented, it is anticipated that the resolution of the spectrograph will be limited either by source size, for studies using thin emitting layers embedded in 200-μm- to 300-μm-diameter CH spheres, or by the intrinsic limits of the crystal, as in implosion studies of filled microballoons. We expect to test these improvements in the near future.

ACKNOWLEDGMENT

This work was supported by the U.S. Department of Energy Office of Inertial Fusion under agreement No. DE-FC08-85DP40200 and by the Laser Fusion Feasibility Project at the Laboratory for Laser Energetics, which has the following sponsors: Empire State Electric Energy Research Corporation, General Electric Company, New York State Energy Research and Development Authority, Ontario Hydro, Southern California Edison Company, and the University of Rochester. Such support does not imply endorsement of the content by any of the above parties.

Muscovite sheets of large size were kindly provided by Dr. Barry Luther-Davies of the Australian National University, Department of Engineering Physics.

REFERENCES

1. Good general references to the use of x-ray spectroscopy in plasma diagnosis include: M. H. Key and R. J. Hutcheon, *Adv. At. Mol. Phys.* **16**, 201 (1980); C. DeMichelis and M. Mattioli, *Nucl. Fusion* **21**, 677 (1981).
2. See, for example: S. R. Stone and J. C. Weisheit, LLNL Report UCID-20262 (1984).
3. M. D. Rosen *et al., Phys. Rev. Lett.* **54**, 106 (1985); D. L. Matthews *et al., ibid.* **54**, 110 (1985); J. F. Seely, C. M. Brown, U. Feldman, M. Richardson, B. Yaakobi, and W. E. Behring, *Opt. Commun.* **54**, 289 (1985). For a general review of the short-wavelength laser approach, see R. W. Waynant and R. C. Elton, *Proc. IEEE* **64**, 1058 (1976); F. V. Bunkin, V. I. Derzhiev, and S. I. Yakovlenko, *Kvant. Elektron. (Moscow)* **8**, 1621 (1981) [*Sov. J. Quantum Electron.* **11**, 981 (1981)].
4. For description of streak spectrometers, see, for example: LLE Review **14**, 16 (1983); M. H. Key *et al., Phys. Rev. Lett.* **44**, 1669 (1980).
5. See, for example: B. L. Henke, J. P. Knauer, and K. Premaratne, *J. Appl. Phys.* **52**, 1509 (1981).
6. P. A. Jaanimagi and B. L. Henke (to be published).
7. G. I. Brukhnevitch, V. K. Cevokin, Yu. S. Kasyanov, V. V. Korobkin, A. A. Malyutin, A. M. Prokhorov, M. C. Richardson, M. Ya. Schelev, and B. M. Stepanov, *Phys. Lett.* **51A**, 249 (1975).
8. L. Von Hamos, *Z. Kristallogr.* **101**, 17 (1939); C. B. Van Den Berg and H. Brinkman, *Physica* **21**, 85 (1955).
9. B. Yaakobi, R. E. Turner, H. W. Schnopper, and P. O. Taylor, *Rev. Sci. Instrum.* **50**, 1609 (1979).
10. B. Yaakobi and V. Bhajavatula, LLE Report No. 89 (1979).
11. B. J. MacGowan, in Annual Report to the Laser Facility Committee, Rutherford Appleton Report RL-82-039, 1.28–1.30 (1982).
12. N. H. Burnett *et al., Phys. Rev. A* **29**, 2294 (1984).
13. T. A. Hall, *J. Phys. E* **17**, 110 (1984).
14. A. Hauer, J. D. Kilkenny, and O. L. Landen, *Rev. Sci. Instrum.* **56**, 803 (1985); P. Kirkpatrick and A. V. Baez, *J. Opt. Soc. Am.* **33**, 766 (1948).
15. B. Yaakobi and A. J. Burek, *IEEE J. Quantum Electron.* **QE-19**, 1841 (1983).
16. It is not possible to construct a collecting-crystal spectrograph with an image axis perpendicular to the radius to the target and still retain the geometry for mosaic focusing found in the Von Hamos design.
17. R. S. Marjoribanks and M. C. Richardson (to be published).

18. For cones of smaller angle, it might be expected that this performance would be improved.

19. P. A. Jaanimagi and M. C. Richardson, *Rev. Sci. Instrum.* **27**, 1095 (1983).

20. V. A. Boiko, S. A. Pikuz, and A. Ya. Faenov, *J. Phys. B* **12**, 1889 (1979); E. V. Aglitskii, V. A. Boiko, A. V. Vinogradov, and E. A. Yukov, *Sov. J. Quantum Electron.* **4**, 322 (1974); see also reference 1.

Section 3
ADVANCED TECHNOLOGY DEVELOPMENTS

3.A Ultrafast Device Characterization — The Five-Picosecond Transistor

As switching speeds of microelectronic circuits increase, new problems arise in characterizing them. It is now typical for a new device to be faster than direct, conventional measurement techniques. Some insight can still be gained from indirect measurements.

One such technique is the ring oscillator. With this technique, 10, 20, or more devices are connected in a ring configuration, and the entire ring is made to oscillate at its maximum frequency. The individual device response is then taken to be the period of oscillation divided by the number of devices in the ring. The large number of devices tends to average out individual device characteristics. In addition, connections between the devices start affecting the overall response. As the individual device response becomes faster, these effects become more pronounced.

Another technique commonly employed is gain measurement in the frequency domain. Here a single device is used as an analog amplifier, and the gain, as a function of frequency, is measured. While this measurement is useful in analog applications of transistors, the relationship between frequency response and time-domain response is not exact. Here, too, the difficulties with increasing device speed become more pronounced. Generally, measurements can be made from dc to about 26 GHz using commercial connectors. Beyond this frequency, measurements are made in narrow frequency bands, using a separate apparatus for each band. In addition, each apparatus is optimized for

operation in that particular frequency band. Eventually, however, the high-frequency response is linearly extrapolated from the highest measured frequencies.

Direct measurement can, however, be achieved through the electro-optic sampling technique. First developed at LLE in 1982,[1] this technique takes advantage of the advances made in ultrashort laser-pulse technology. The LLE system was a colliding-pulse mode-locked (CPM) laser, which routinely emits pulses of less than 100-fs FWHM. These short optical time intervals permit a direct measurement of electrical signals with rise times of a few hundred femtoseconds.[2]

Recently, this technique has been applied to the characterization of several new types of devices such as the two-dimensional electron gas field-effect transistor (TEGFET) and the metal semiconductor field-effect transistor (MESFET).[3] Although still tractable by the indirect techniques described above, their device rise times of 16 and 25 ps, respectively, represent switching speeds beyond the capacity of conventional direct measurement.

One device, however, resists even indirect attempts at characterization: the permeable-base transistor (PBT). Conceived at MIT Lincoln Laboratory in 1979,[3] the PBT presents unique problems in its manufacture. As shown in Fig. 26.20, a PBT is arranged similarly to a vacuum-tube triode, except that here the "grid" has submicrometer dimensions. By interrupting the GaAs growth process to fabricate the grating, contaminants are introduced, which keep yields low. As of this writing, only

Fig. 26.20
Geometry of the permeable-base transistor (PBT).

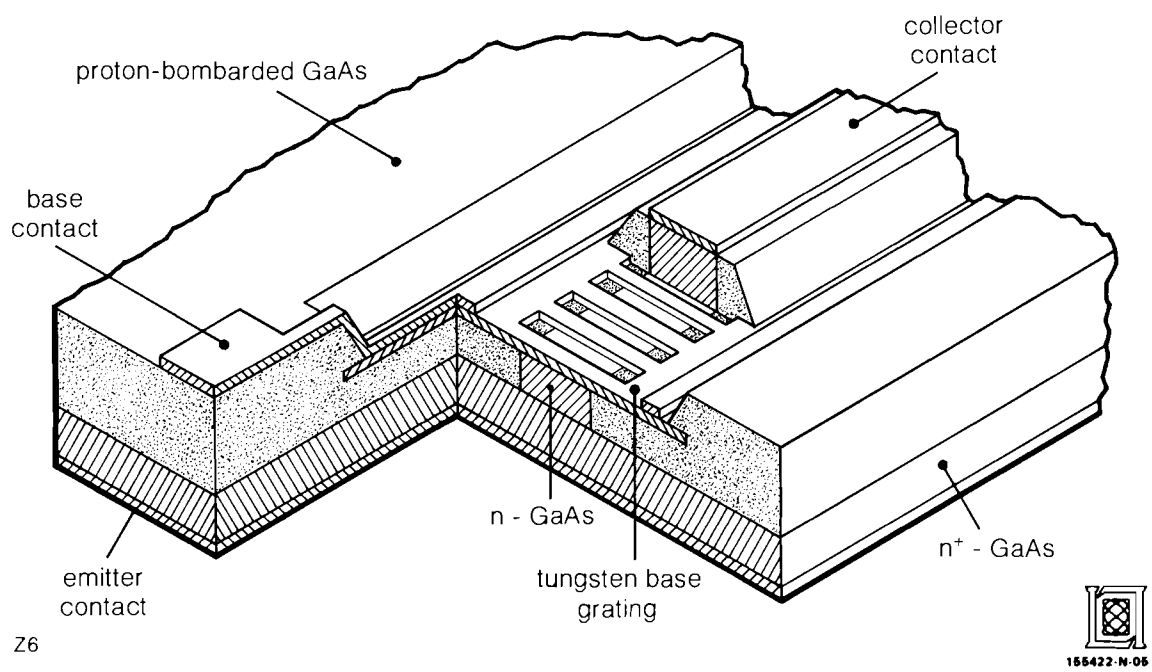

single devices have been fabricated. With only single, discrete devices available, ring oscillators cannot be fabricated. In addition, the analog measurements have proved very difficult because of the very high gain of the PBT. The device is now known to oscillate at maximum frequencies above 200 Ghz.[4] An example of the frequency versus gain characteristics for several wafers of PBT's is shown in Fig. 26.21. The very nonlinear response is due to the interaction between the device and the experimental apparatus. Curve HiP2 was truncated before the onset of fixture resonances. The speed of this device results from advances in fabrication techniques that allow for extremely small dimensions in both the horizontal and vertical directions. These advances have led to a device that until now remained completely uncharacterized in the time domain.

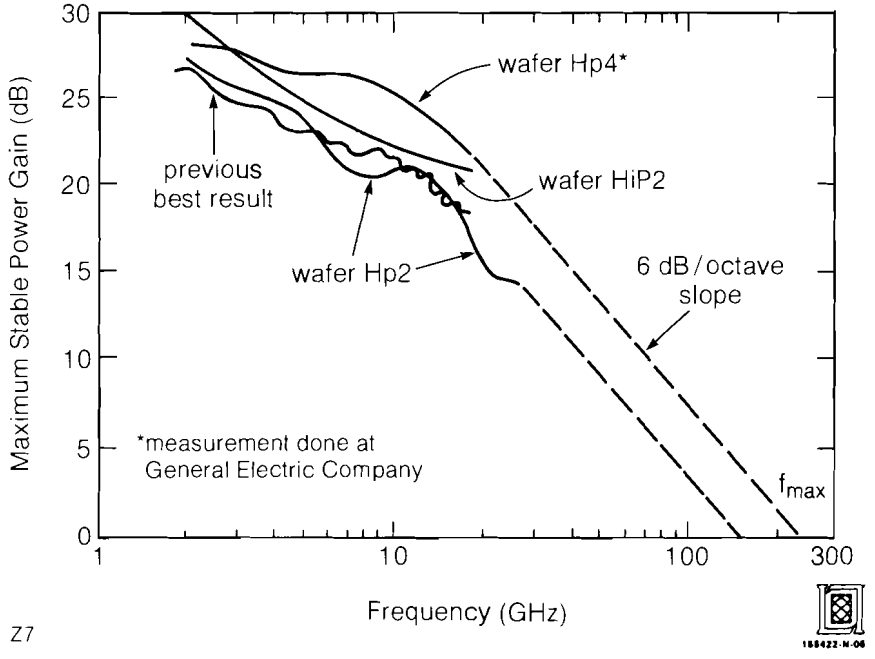

Fig. 26.21
Frequency versus gain measurements for various PBT wafers. The PBT tested was from wafer Hp4.

For electro-optic characterization, the PBT was built into the sampling geometry shown in Fig. 26.22. This geometry permits dc biasing as well as high-speed operation. The CPM-laser-based sampling system measured the rise time, as shown in Fig. 26.23. Electromagnetic radiation from the input connection was thought to cause the negative prepulse. This feature did not scale in amplitude with PBT gain. It has also been present in earlier measurements on TEGFET and MESFET devices. The gain of the PBT is shown, as a function of applied voltage, in Fig. 26.24.

This measurement identifies, to the best of our knowledge, the currently fastest three-terminal room-temperature device. It also represents a benchmark measurement, since from now on faster devices can only be measured effectively by electro-optic techniques.

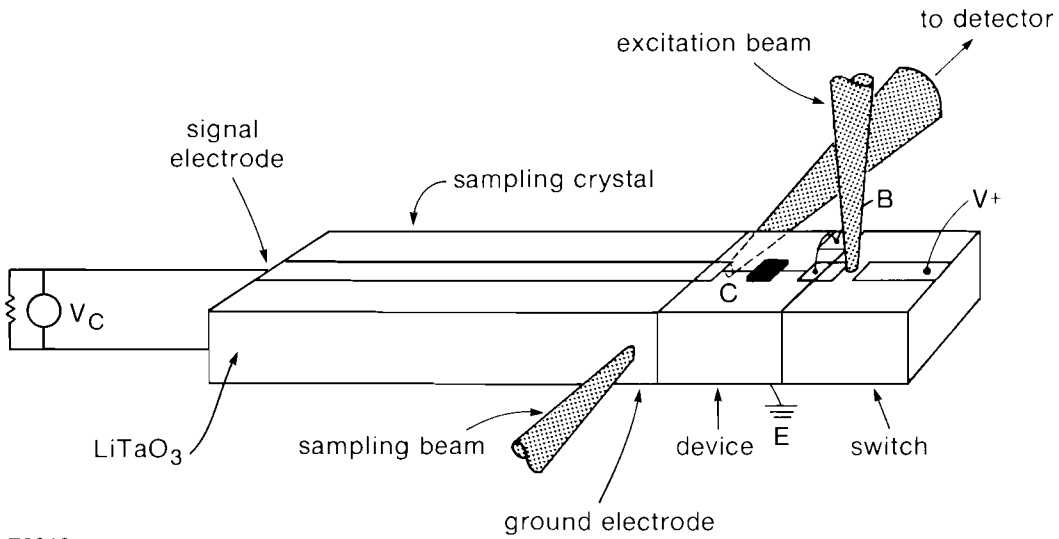

Fig. 26.22
Sampling geometry for PBT characterization. Looping wire bonds were used for bias leads to prevent loading of high-speed signal paths.

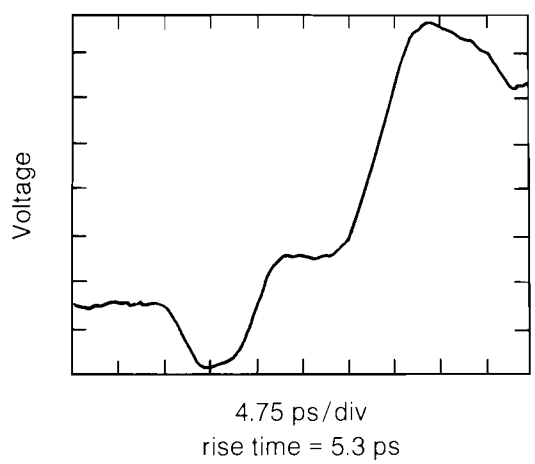

Fig. 26.23
Step response of PBT as measured by the electro-optic sampling system.

ACKNOWLEDGMENT

This work was supported by the Laser Fusion Feasibility Project at the Laboratory for Laser Energetics, which has the following sponsors: Empire State Electric Energy Research Corporation, General Electric Company, New York State Energy Research and Development Authority, Ontario Hydro, Southern California Edison Company, and the University of Rochester. The PBT development is sponsored by the Defense Advanced Research Projects Agency and Department of the Air Force. Such support does not imply endorsement of the content by any of the above parties.

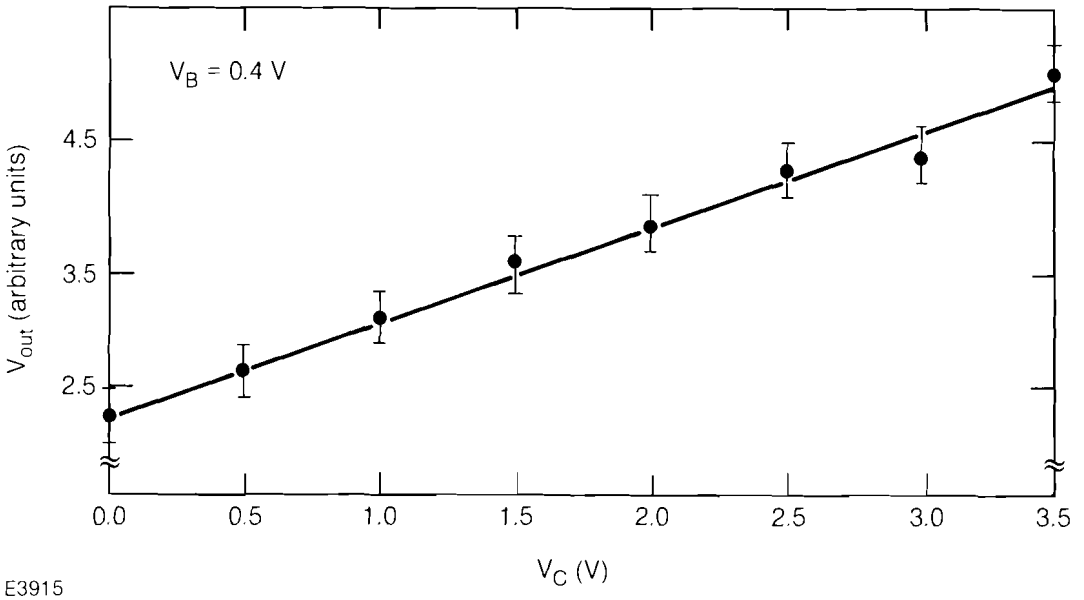

Fig. 26.24
PBT gain as a function of applied voltage. The amplitude was measured using the electro-optic sampling system.

REFERENCES

1. J. A. Valdmanis, G. Mourou, and C. W. Gabel, *Appl. Phys. Lett.* **41**, 211 (1982).
2. K. E. Meyer, D. R. Dykaar, and G. A. Mourou, in *Picosecond Electronics and Optoelectronics*, edited by G. A. Mourou, D. M. Bloom, and C. H. Lee (Springer-Verlag, Berlin, Heidelberg, New York, and Tokyo, 1985), p. 54.
3. C. O. Bozler *et al.*, in *Proc. 7th Bien. Cornell Conf. on Active Microwave Devices*, p. 33 (1979).
4. M. A. Hollis *et al., Technical Digest IEDM*, p. 102 (1985).

3.B Nodular Defects in Optical Coatings

Damage in transport optics for high-peak-power lasers often occurs first at defect sites in optical coatings. A characteristic defect in coatings is the nodule. It causes scattering and moisture penetration; in high-energy laser coatings, the localized stress,[1] localized heat,[2] and microlens effects[3] generated by nodules are assumed to trigger laser-induced damage. Nodular defects are found in various metal and dielectric films that are fabricated by sputtering, chemical vapor deposition, electroplating, thermal evaporation (both electron beam and thermal resistive), and ion plating.

A number of reports have focused on this microstructure during the last 15 years. K. Guenther[4] outlined the importance of the nodule in

optical coatings. Nodular defects[5] were thought to be formed by the same self-shadowing effects that cause columnar structure.[4,5] However, this effect alone could neither explain the nodular growth in films deposited at normal incidence nor the peculiar shapes of nodules. This report investigates the character, formation, and development of nodular defects in thin films. Computer simulation and experimental verification of nodule growth are emphasized.

By using a modified version of the hard-disk model, this simulation maintains the simplicity that is essential in simulating film growth on a large scale (up to 120,000 deposited disks). The modified model can accommodate different deposition conditions and material properties and thereby link the growth of nodules to these conditions.

The starting point of these calculations is the two-dimensional hard-disk model of Dirks and Leamy,[6] in which disks fall randomly onto the surface and then stick where they land or come to rest in the nearest pockets, where each disk is supported by two other disks that had arrived earlier. Results from this model reproduce well the experimentally found appearance of columnar microstructure and columnar tilt in thin films. The model best reproduces low-density films and inherently favors hexagonal, close-packed structures. However, it fails to take account of complex adsorption processes that influence film-structure evolution. During actual condensation, an adatom or admolecule moves some distance over the surface after impact because of transverse momentum conservation and thermal diffusion.[7] This migration of adatoms and admolecules depends critically on substructure temperature, kinetic energy of incident particles, residual-gas content, surface topography, and adatom and admolecule activation energies.

The modified model (Fig. 26.25)[8,9] includes the migration process by allowing an incident disk to migrate across the surface by jumping from site to site until an eligible site is reached. A probability-density distribution is established for the likelihood of a newly arriving disk undertaking 1, 2, or n jumps after impact and before coming to rest. R_1, R_2 . . . R_n are the probabilities for 1, 2 . . . n sequential jumps, satisfying

$$\sum_{j=1}^{n} R_j = 1 . \qquad (1)$$

The migration parameter λ combines this probability density with the average distances covered by the jumping disks for 1, 2 . . . or n jumps:

$$\lambda = 0.6\, R_1 + 1.6\, R_2 + \quad . \quad . \quad . \quad + a_n R_n \quad , \qquad (2)$$

where the coefficients a_n are the average distances traveled by the disks. These distances are derived from a separate set of simulations. In simulating different adatom-mobility conditions, a suitable value for the migration parameter λ is chosen, and restrictions are imposed on the probability distribution in order to come up with a set of values for the R_n.

Molecular dynamics models of surface effects, such as film growth or roughening, often use a Lennard-Jones interaction potential in describing the forces among the lattice constituents. Here a simplified representation of this potential is chosen for reasons of computational speed. It constitutes a compromise between the simplest hard-disk interaction – i.e., one in which the attractive force is constant up to twice a disk radius and in which the disks have to touch before the force acts – and the computationally unwieldy, full Lennard-Jones interaction. This code uses a constant force that is truncated in range by an adjustable extension factor that is heuristically set between 1 and 1.75. Disks passing within this extended capture length are attracted to the fixed disks.

The film-growth simulation code has been implemented on IBM-XT and HP 9000-200 microcomputers. By adjusting various parameters one can create a coating with nodules in "controlled conditions." Experiments in support of the simulation activities used Al_2O_3 grains, whose diameters were larger than 0.05 μm, as seeds for nodule growth on polished glass surfaces. The seeded substrates were overcoated with either a single layer of ZnS or multilayer Ta_2O_5–SiO_2 stacks. Both normal incidence on stationary substrates and various oblique-incidence angles for rotating substrates were explored. The samples were fractured, and coating cross sections were examined by SEM.

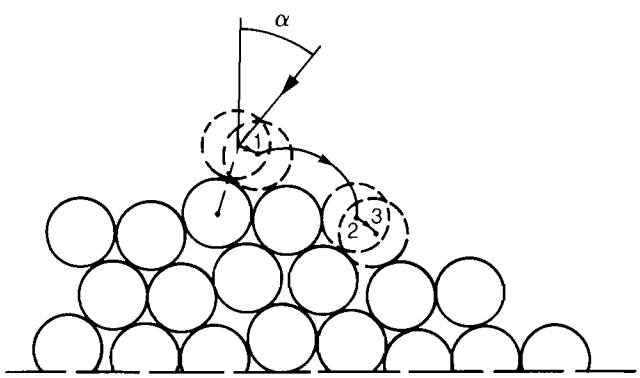

α = vapor incidence angle
λ = average distance jumped by hard disks

G1625

Fig. 26.25
Modified hard-disk model allows multiple jumps of an adatom after it impinges on the substrate. In this example, the adatom was allowed to jump three times before coming to rest.

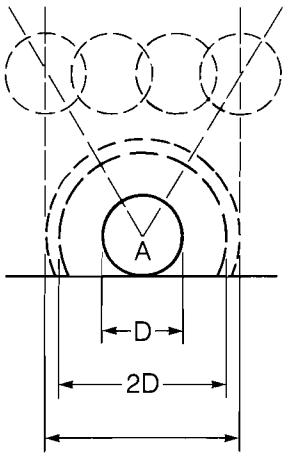

2D × extending factor

G1755

Fig. 26.26
An approximate potential is implemented by extending the capture length of an adatom. In the hard-disk model, the capture length is just two times the radius of the adatom. In our model, we extend this length by a factor ranging from 1 to 1.75.

The Self-Extending Effects of Clusters and Nodules

Almost all nodule shapes found in thin films are characterized by an inverted cone with a dome or egg-like top. Their diameter increases monotonically with film thickness. Such nodule-like growth occurs even when the effects of the surrounding film are ignored. In this case we refer to the isolated growth structures as clusters. Nodules and clusters show self-extension, which can be examined by varying the capture length during the growth process.

A disk, A, has a capture length greater than its diameter, as shown in Fig. 26.26. Newly arriving disks within this capture length will impinge upon A such that the cluster starting at disk A extends its diameter during growth and forms a cone regardless of specific seed size or adatom mobility. The cone angle of clusters that form on an individual disk is $36° \pm 2°$ at $\lambda = 0$, as shown in Fig. 26.27(a), and is almost the same result as P. Ramanlal's disk fan.[10] The cone angles vary from 30°–40° if clusters initiate at larger-circle seeds [Fig. 26.27(b)].

The effects of extending the capture length, when adatom mobility is accounted for, are seen in Figs. 26.27(c) and 26.27(d). The increase in mobility results in a decrease of the cone angle of the cluster when the capture length is not extended. However, if the capture length of the disks is extended, the nodule cone angle of the cluster increases. This suggests that longer-range attractive forces between atoms produce larger cone angles.

Clusters forming simultaneously and in close proximity to one another on a smooth substrate will not initiate the self-extending process in the computer simulations because of competition among adjacent clusters. Nodules do not form spontaneously from homogeneous nucleations on a smooth substrate surface for the same reason. Only those clusters that start at protrusive seeds have chances to develop the nodule shapes.

The Geometry of Nodule Growth

A growth simulation of a nodule on a stationary substrate is shown in Fig. 26.28(a). The structure is characterized by straight sides similar to those of Fig. 26.28(b) (single layer of ZnS) and Fig. 26.28(c) (multilayer of Ta_2O_5-SiO_2). The nodule cone angle in Fig. 26.28(c) is 42°, close to the one with an extending factor 1.5 in Fig. 26.27(d). The thickness of the simulated film in Fig. 26.28(a) is about 1700 Å if a disk represents an atom of diameter 5 Å.

Figure 26.29(a) is a simplified case of the initial stage of cluster growth on a rotating substrate with oblique vapor incidence ($\alpha = 50°$). Any point on the nodule side is exposed to the incident flux during half of a rotation period so that the seed grows with a cone angle 2γ. J is the incident flux and the cone angle γ satisfies

$$\tan\gamma = \frac{\int_{-\pi/2}^{\pi/2} J \sin(\alpha - \gamma)\, d\phi}{\int_{0}^{2\pi} J \cos\alpha\, d\phi} \tag{3}$$

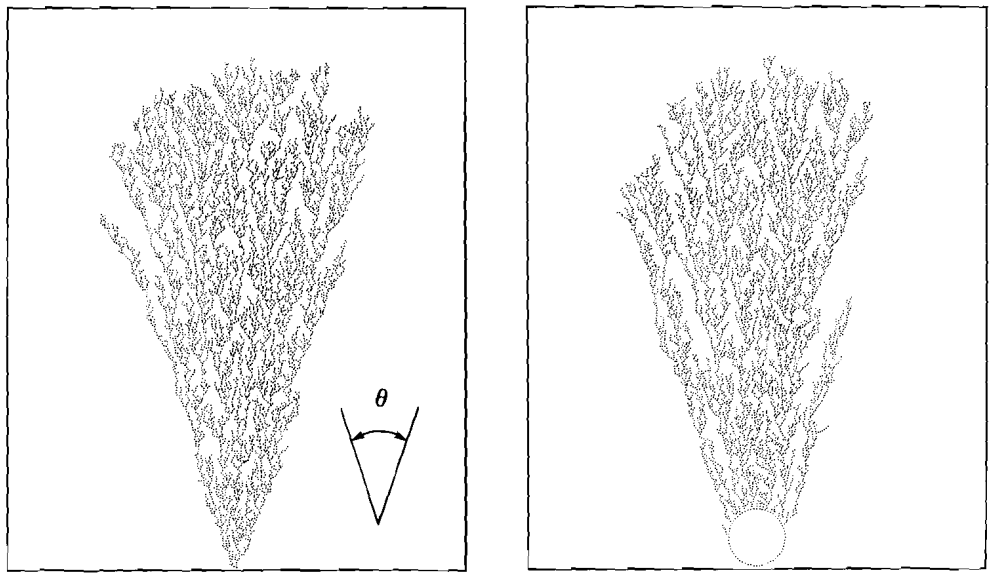

(a) nucleus: single disk
$\lambda = 0$, $\theta = 36° \pm 2°$

(b) nucleus: circle
$\lambda = 0$, $\theta = 30° \sim 40°$

G1626

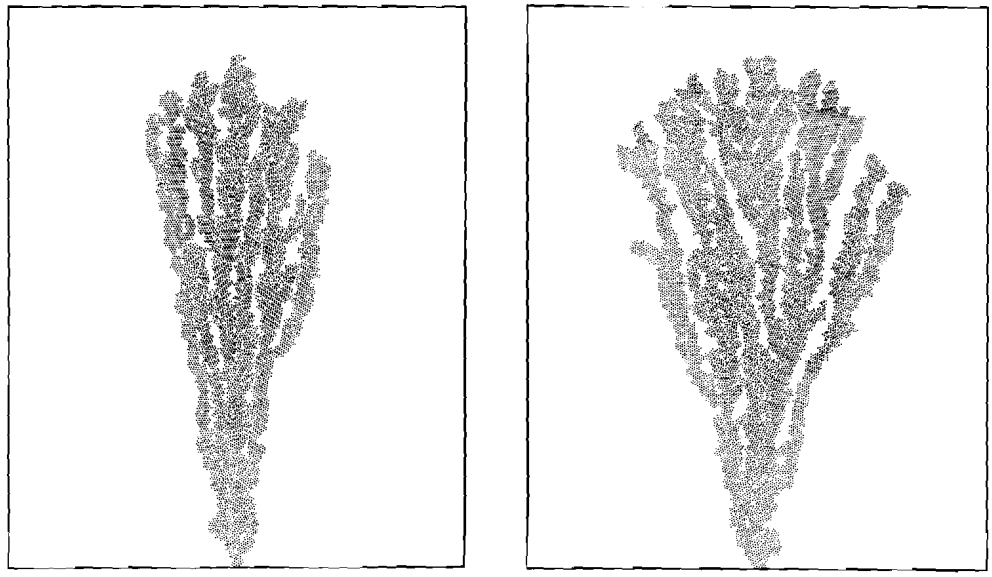

(c) $\lambda = 1.9$, $\theta = 20°$
extending factor = 1.0

(d) $\lambda = 2.0$, $\theta = 45°$
extending factor = 1.5

G1627

Fig. 26.27
Development of the model for simulating cluster growths in "free space." Growths with low adatom mobility are seen in (a) and (b), where the nucleus is a single adatom and a larger circle. Repeated trials of (a) gave consistent values for the cone angle. Allowing some adatom mobility results in a lower cone angle (c). Extension of the capture length (d) increases the cone angle.

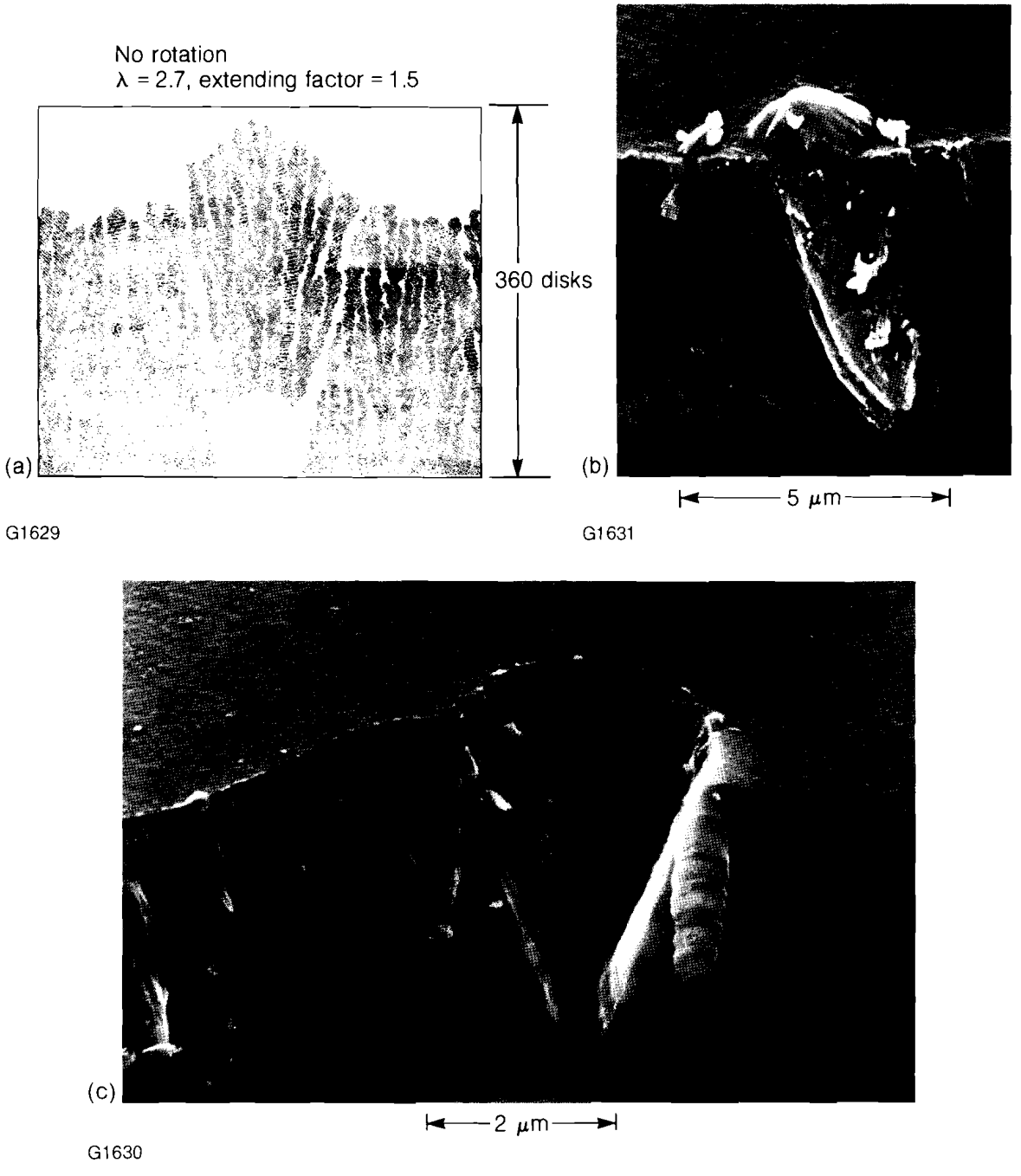

Fig. 26.28
The characteristic shape of a nodule formed on a fixed substrate with normal vapor incidence is an inverted cone. The model (a) is supported by experiment with single (b) and multiple (c) layer films.

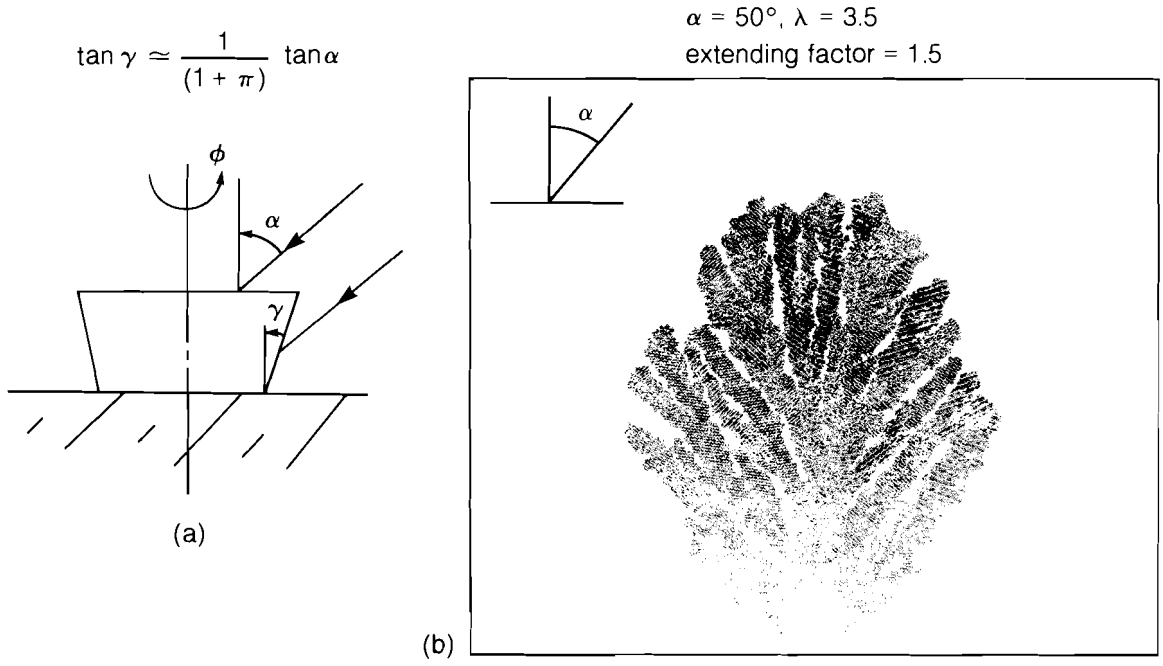

Fig. 26.29
Rotation of the substrate and an oblique vapor incidence results in an increase in the nodule cone angle. The simulation in (b) shows this effect for a nodule without the restrictive influence of the surrounding film. This is typical for the initial stages of nodule growth.

For small γ, the approximation holds

$$\tan\gamma \simeq \frac{1}{(1+\pi)} \tan\alpha . \qquad (4)$$

Equation (3) establishes the relation between α and γ in a cluster forming on a rotating substrate. An increase in the incident angle α results in a corresponding increase in the cone angle γ. A cluster enlarges its diameter rapidly [Fig. 26.29(b)] during the early growth stage. In fact, Eq. (3) holds only at the initial stage of coating growth. After the step around a seed disappears and the dome on top of the nodule forms, the increase in nodule diameter slows down. As a result, a bowl-like bottom or parabolic sides evolve, in contrast to the straight sides of the nodules grown under normal incident flux on stationary substrates. Nodules in a coating deposited by a wide source (i.e., sputtering) exhibit similar shapes due to the spread in angle of incident particles typical for such a condition. Figures 26.30(a) and 26.31(a) are two nodule simulations for rotating substrates (on axis). Note that the diameter of the nodule grown at an angle of incidence α = 70° is much larger than that at α = 50°. In Figs. 26.30(b) and 26.30(c) as well as Figs. 26.31(b) and 26.31(c), experimental test specimens are shown for comparison. Although the scale lengths are orders of magnitude different between simulations [Figs. 26.30(a) and 26.31(a)] and the corresponding micrographs [(b) and (c) of both figures], the visual agreement in geometry is quite good.

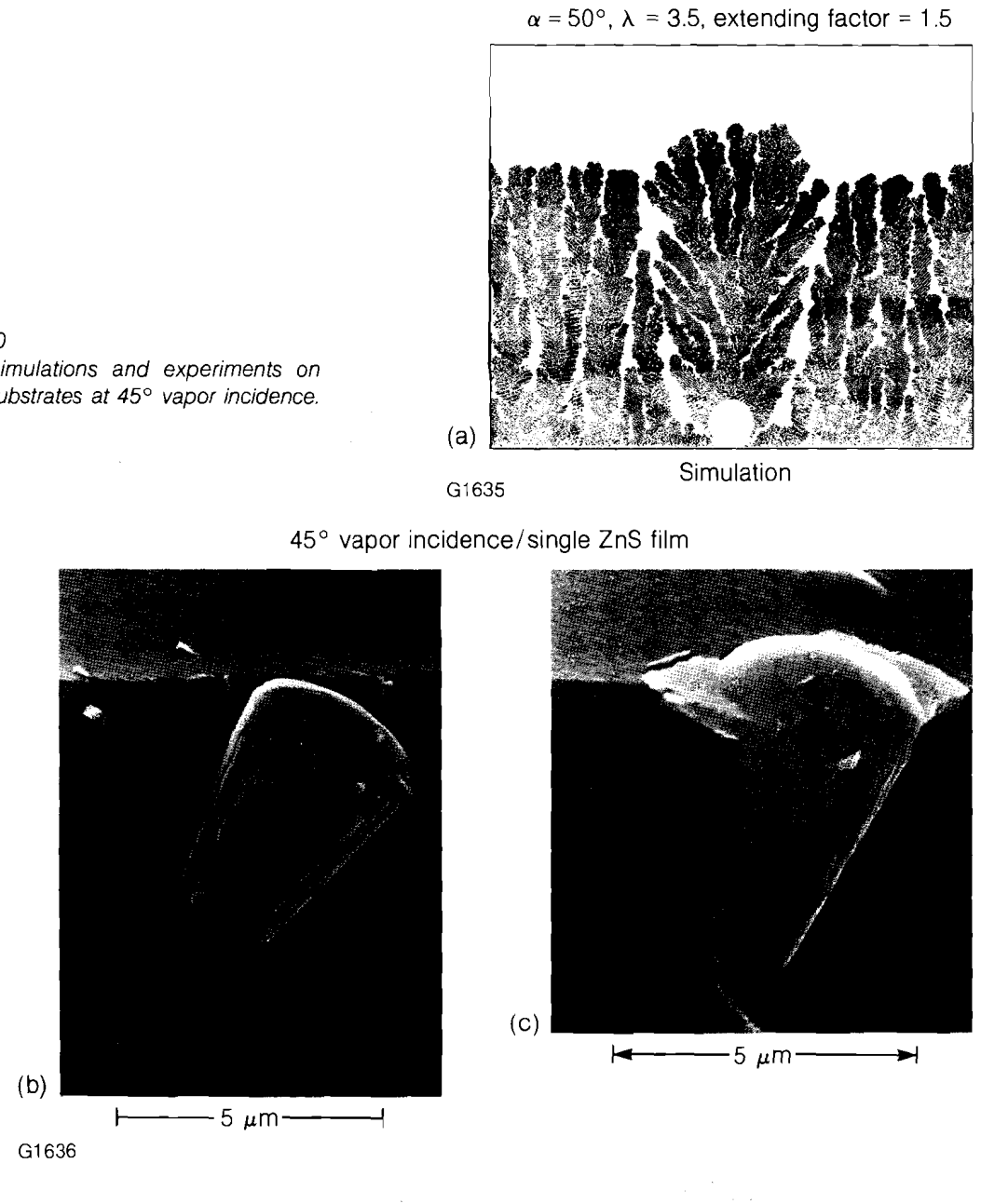

Fig. 26.30
Nodule simulations and experiments on rotating substrates at 45° vapor incidence.

A seed is a necessary condition for a nodule to form. However, while larger seeds tend to generate larger nodules in simulations, not all seeds will grow into nodules. We find, for instance, that a seed of three-disk diameter fades into the film without nodule formation during growth at normal incidence. At sufficient adatom mobility (λ = 3.4), disks migrate longer distances along the surface and fill the volume around the small seed. Larger imperfections, such as dust, polishing residue, and rough protrusions on substrate surfaces, all act as starting points for nodules. Smaller defects on substrates, such as impurities, scratches,

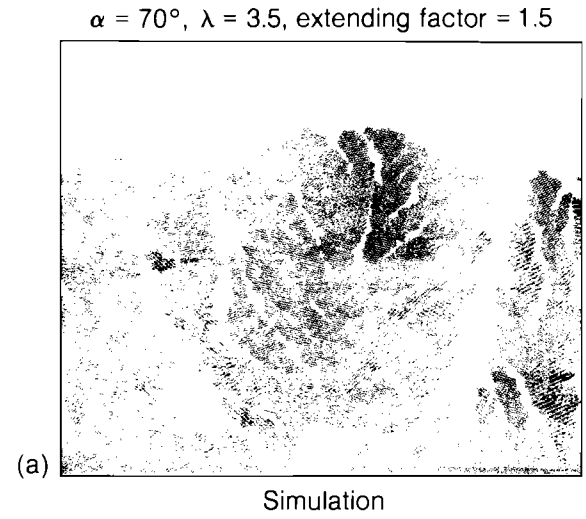

Fig. 26.31
Nodule simulations and experiments at 70° vapor incidence. The size of the nodules varied significantly at this vapor angle.

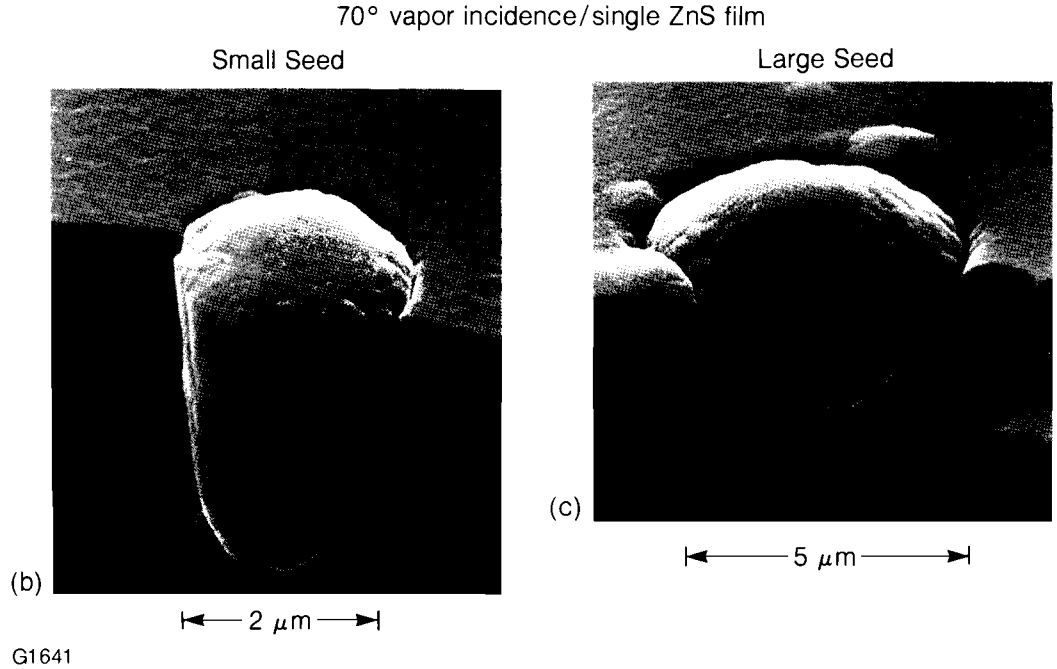

steps, and ledges, are preferred nucleation sites and may develop into seeds for nodules under suitable condensation conditions.

Figure 26.32 shows the simulation for a three-layer film containing a nodule that initiated at a spatter site in the first layer. It also shows the nodule growth through the layer interfaces.

The shadowing effect of a nodule produces an empty area around it during growth that causes a gap if addisks are not activated into filling

the volume. These gaps, which amount to 50 Å to 100 Å in corresponding simulations, depending on mobility, can be clearly seen around large nodules in the SEM micrographs of the film cross sections [Figs. 26.31(b) and 26.31(c)]. These gaps represent a significant break in a film's continuity. They also impede thermal conductance away from the nodule if, under high-power laser irradiation, the nodule's absorption should cause local heating.

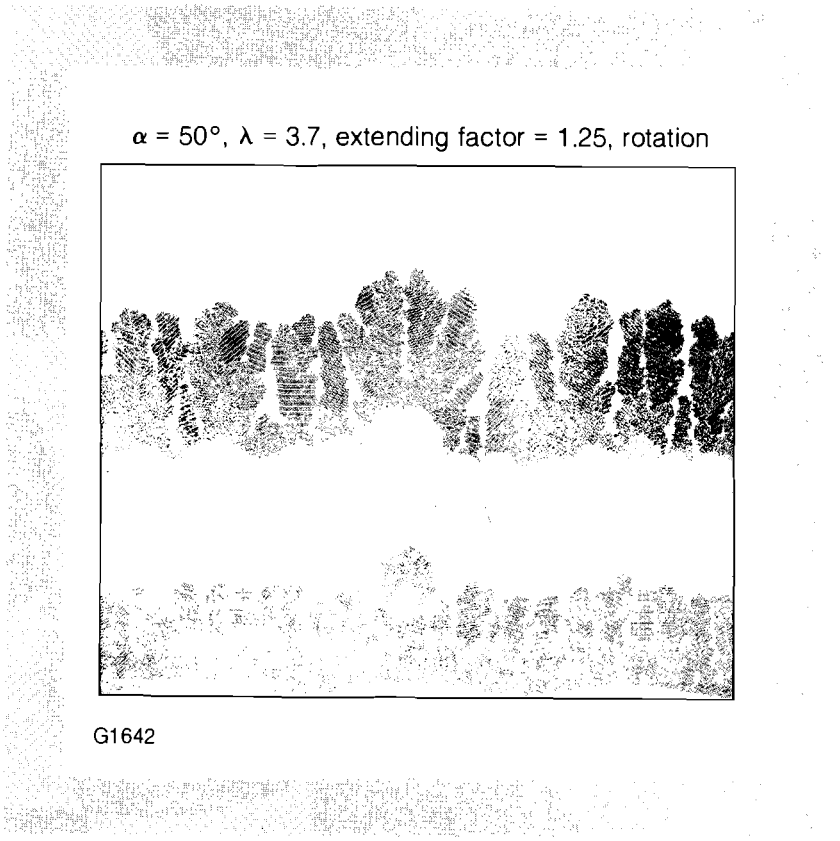

Fig. 26.32
Particles thrown up from the evaporant can act as nuclei for nodules. The nodule seen here also propagates up through a multilayer.

ACKNOWLEDGMENT

This work was supported by the New York State Center for Advanced Optical Technology of The Institute of Optics and the sponsors of the Laser Fusion Feasibility Project at the Laboratory for Laser Energetics, which has the following sponsors: Empire State Electric Energy Research Corporation, General Electric Company, New York State Energy Research and Development Authority, Ontario Hydro, Southern California Edison Company, and the University of Rochester. Such support does not imply endorsement of the content by any of the above parties.

REFERENCES

1. T. Spalvins and W. A. Brainard, *J. Vac. Sci. Technol.* **11**, 1186 (1974).
2. K. H. Guenther, *Appl. Opt.* **23**, 3806 (1984).
3. J. Murphy, *Contemporary Infra-Red Sensors and Instruments* (SPIE, Bellingham, WA, 1980), Vol. 246, p. 64.
4. K. H. Guenther, *Appl. Opt.* **20**, 1034 (1981).
5. J. W. Patten, *Thin Solid Films* **63**, 121 (1979).

6. A. G. Dirks and H. J. Leamy, *Thin Solid Films* **47**, 219 (1977).

7. K. L. Chopra, *Thin Film Phenomena* (McGraw-Hill, New York, 1969), Chap. 4.

8. Liao Bangjun and H. A. Macleod, *Proceedings of the Southwest Conference on Optics* (SPIE, Bellingham, WA, 1985), Vol. 540, #TA 118.

9. Liao Bangjun and H. A. Macleod (to be published).

10. P. Ramanlal and L. M. Sander, *Phys. Rev. Lett.* **54**, 1828 (1985).

Section 4
NATIONAL LASER USERS FACILITY NEWS

During the second quarter of FY86, two series of NLUF experiments were run on OMEGA and the NLUF steering committee met to review proposals for FY87.

NLUF experiments during this quarter carried out by **J. Seely, U. Feldman,** and **C. Brown** (Naval Research Laboratory) and **W. Behring** (NASA-Goddard Space Flight Center) continued investigations of the XUV and x-ray spectroscopy of high-Z ions. In one series of shots on Au-coated targets, the Fe I, Co I, Cu I, and Zn I isoelectronic sequences of Au (Z-79) were recorded. This is a considerable extension of previous work in which these transitions had been observed only for elements with atomic number Z = 66 and below. In other experiments during this period, spectra from Bi and U targets were also obtained.

In a collaborative effort with LLE scientists, **D. Duston** (SDIO/NRL) and A. **Hauer** (LANL) conducted the first series of experiments on dielectronic satellites of Ar x-ray line emission from compressed targets. The glass targets used in these experiments were fabricated at LANL and were fueled with Ar and D_2 and overcoated with several microns of CH. Time-integrated as well time-resolved spectra of the x-ray emission were obtained; these data are now being analyzed.

On 28 February 1986, the NLUF Steering Committee met to review 15 proposals submitted for the FY87 funding cycle. The Committee reviewed and ranked the proposals for facility time and DOE funding.

Proposals for consideration for the FY88 funding cycle are due by 15 December 1986.

For more information regarding proposal guidelines and the resources available at the National Laser Users Facility, please contact:

Manager
National Laser Users Facility
Laboratory for Laser Energetics
University of Rochester
250 East River Road
Rochester, New York 14623-1299
(716) 275-2074

ACKNOWLEDGMENT

This work was supported by the U.S. Department of Energy Office of Inertial Fusion under agreement No. DE-FC08-85DP40200.

PUBLICATIONS AND CONFERENCE PRESENTATIONS

Publications

Theodore Sizer II and Michael G. Raymer, "Modification of Atomic Collision Dynamics by Intense Ultrashort Laser Pulses," *Phys. Rev. Lett.* **56**, 123–126 (1986).

R. Epstein, S. Skupsky, and J. Delettrez, "Effects of Non-Maxwellian Electron Populations in Non-LTE Simulations of Laser-Plasma Thermal Transport and Implosion Experiments," *J. Quant. Spectrosc. Radiat. Transfer* **35**, 131–143 (1986).

M. C. Richardson, R. Epstein, O. Barnouin, P. A. Jaanimagi, R. Keck, H. Kim, R. S. Marjoribanks, S. Noyes, J. M. Soures, and B. Yaakobi, "Multibeam Laser-Imploded Cylindrical Plasmas," *Phys. Rev. A* **33**, 1246–1253 (1986).

R. Epstein and R. S. Craxton, "Statistical Ray Tracing in Plasmas with Random Density Fluctuations," *Phys. Rev. A* **33**, 1892–1902 (1986).

G. G. Gregory, S. A. Letzring, M. C. Richardson, and C. D. Kiikka, "High Time-Space Resolved Photography of Laser Imploded Fusion Targets," in *High Speed Photography, Videography, and Photonics III* (SPIE, Bellingham, WA, 1985), Vol. 569, pp. 141–148; P. A. Jaanimagi, B. L. Henke, and M. C. Richardson, "An Absolutely Calibrated Time-Resolving X-Ray Spectrometer," *ibid.*, pp. 159–166; M. C. Richardson, G. G. Gregory, S. A. Letzring, R. S. Marjoribanks, B. Yaakobi, B. L. Henke, P. A. Jaanimagi, and A. Hauer, "Time-Resolved X-Ray Spectrographic Instrumentation for Laser Fusion and X-Ray Laser Studies," *ibid.*, pp. 149–158.

R. L. McCrory and J. M Soures, "Laser Fusion Experiments at the University of Rochester," *Nucl. Fusion* **25**, 1367–1372 (1985).

D. Strickland and G. Mourou, "Compression Amplified Chirped Optical Pulses," *Opt. Commun.* **56**, 219–221 (1985).

R. L. McCrory, "Inertial Confinement Fusion (ICF)," *Phys. Today*, S-61–S-62 (January 1986).

F. J. Marshall, D. A. Hardy, A. Huber, J. Pantazis, J. McGarity, E. Holeman, and J. D. Winningham, "Calibration System for Electron-Detectors in the Energy Range from 10 eV to 50 keV," *Rev. Sci. Instrum.* **57**, 229–235 (1986).

J. A. Valdmanis and G. Mourou, "Subpicosecond Electro-Optic Sampling: Principles and Applications," *IEEE J. Quantum Electron.* **QE-22**, 69–78 (1986).

J. A. Valdmanis and G. Mourou, "Electro-Optic Sampling: Testing Picosecond Electronics, Part I, Principles and Embodiments," *Laser Focus*, 96–106 (February 1986); "Electro-Optic Sampling: Testing Picosecond Electronics, Part 2, Applications," *ibid.*, 84–96 (March 1986).

S. Williamson, G. Mourou, and J. C. M. Li, "Time-Resolved Laser-Induced Phase Transformation in Aluminum," in *Energy Beam-Solid Interactions and Transient Thermal Processing/1984 Symposium* (Material Research Society, Pittsburgh, PA, 1985), pp. 87–96.

Forthcoming Publications

S. D. Jacobs, "Liquid Crystal Devices for Laser Systems," to be published in the *Journal of Fusion Energy.*

B. Yaakobi, R. D. Frankel, J. M. Forsyth, and J. M. Soures, "Laser-Generated X-Ray Source for Time-Resolved Biological and Material Structure Studies," to be published in the *Proceedings of a Symposium on New Methods in X-Ray Absorption, Scattering, and Diffraction.*

The following papers are to be published in the *Proceedings of the Workshop on Physics of Laser Fusion*, Vancouver, B.C., June 1985 (*Canadian Journal of Physics*):

A. Simon, "Raman Scattering."

J. Delettrez, "Thermal Electron Transport in Direct-Drive ICF."

L. M. Goldman, "The Use of Laser Harmonic Spectroscopy as a Target Diagnostic."

The following papers are to be published in the *Journal of Vacuum Science and Technology A:*

R. Q. Gram, H. Kim, J. F. Mason, and M. Wittman, "Ablation Layer Coating of Mechanically Nonsupported Inertial Fusion Targets."

H. Kim, S. Noyes, M. C. Richardson, and B. Yaakobi, "Fabrication of Thin Cylindrical Targets for X-Ray Laser Experiments."

R. Epstein, S. Skupsky, and J. Delettrez, "Effects of Non-Maxwellian Electron Populations in Non-LTE Simulations of Laser-Plasma Thermal and Implosion Experiments," to be published in the *Journal of Quantitative Spectroscopy and Radiative Transfer.*

A. Simon, W. Seka, L. M. Goldman, and R. W. Short, "Raman Scattering in Inhomogeneous Laser Produced Plasma," to be published in *Physics of Fluids.*

A. Hauer, R. D. Cowan, B. Yaakobi, O. Barnouin, and R. Epstein, "Absorption Spectroscopy Diagnosis of Pusher Conditions," to be published in *Physical Review A.*

B. Yaakobi, "X-Ray Diagnostic Methods for Laser Imploded Targets" and "Thermal Transport, Mass-Ablation, and Preheat in Laser-Target Experiments," to be published in the *Proceedings of the Spring College on Radiation in Plasmas*, Trieste, Italy, June 1985 (World Scientific Publishing Co.).

B. Yaakobi, O. Barnouin, C. B. Collins, R. Epstein, A. Hauer, S. Letzring, F. J. Marshall, R. L. McCrory, M. C. Richardson, J. M. Soures, and S. S. Wagel, "Laser-Generated X-Ray Studies Relevant to Compression Diagnostics and Nuclear Level Excitation," to be published in *Laser Interaction and Related Plasma Phenomena* (Plenum Press).

The following papers are to be published in the *Proceedings of the 17th Annual Boulder Damage Symposium*, Boulder, CO, October 1985:

K. A. Cerqua, S. D. Jacobs, B. L. McIntyre, and W. Zhong, "Ion Exchange Strengthening of Nd-Doped Phosphate Laser Glass."

L. Bangjun, D. J. Smith, and B. L. McIntyre, "The Development of Nodular Defects in Optical Coatings."

D. J. Smith, B. Krakauer, C. J. Hayden, A. W. Schmid, and M. J. Guardalben, "Yttrium-Oxide-Based Anti-Reflection Coating for High Power Lasers at 351 nm."

B. Yaakobi, O. Barnouin, M. C. Richardson, and J. M. Soures, "X-Ray Spectroscopic Methods for the Diagnosis of Laser Imploded Targets," to be published in *Review of Scientific Instruments.*

P. A. Jaanimagi, J. Delettrez, M. C. Richardson, and B. Henke, "Temporal Dependence of the Mass Ablation State in UV Laser Irradiation Spherical Targets," to be published in *Physical Review A.*

M. C. Richardson, P. W. McKenty, F. J. Marshall, C. P. Verdon, J. M. Soures, R. L. McCrory, O. Barnouin, R. S. Craxton, J. Delettrez, R. L. Hutchison, P. A. Jaanimagi, R. Keck, T. Kessler, H. Kim, S. A. Letzring, D. M. Roback, W. Seka, S. Skupsky, B. Yaakobi, and S. M. Lane, "Ablatively-Driven Targets Imploded with the 24 UV Beam OMEGA System," in *Laser Interaction and Related Plasma Phenomena Vol. 7,* edited by G. Miley and H. Hora (Plenum Press, New York, in press); M. C. Richardson, G. G. Gregory, R. L. Keck, S. A. Letzring, R. S. Marjoribanks, F. J. Marshall, G. Pien, J. S. Wark, B. Yaakobi, J. D. Goldstone, A. Hauer, G. S. Stradling, F. Ameduri, B. L. Henke, and P. A. Jaanimagi, "Time-Resolved X-Ray Diagnostics for High Density Plasma Physics Studies," *ibid*; W. C. Mead, S. V. Coggeshall, S. R.

Goldman, E. K. Stover, P. D. Goldstone, A. Hauer, V. M. Kindel, L. Montierth, M. C. Richardson, O. Barnouin, P. A. Jaanimagi, R. S. Marjoribanks, R. L. Kauffman, and H. Kornblum, "Analysis, Modeling, and Design of Short Wavelength Laser Plasma Experiments," *ibid.*

The following articles are to be published in *Review of Scientific Instruments*:

M. C. Richardson, P. A. Jaanimagi, L. DaSilva, G. G. Gregory, C. Hestdalen, G. D. Kiikka, and R. Kotmel, "Optical Fiducials for X-Ray Streak Cameras at LLE."

M. C. Richardson, P. G. Burkhalter, D. A. Newman, D. L. Rosen, K. Hudson, and P. Audebert, "Spectral Measurement from Laser Produced Plasmas on OMEGA."

B. Yaakobi, O. Barnouin, M. C. Richardson, J. M. Soures, A. Hauer, and B. Post, "X-Ray Spectroscopic Methods for the Diagnosis of Laser-Imploded Targets."

M. C. Richardson, R. F. Keck, S. A. Letzring, R. L. McCrory, P. W. McKenty, D. M. Roback, J. M. Soures, C. P. Verdon, S. M. Lane, and S. G. Prussin, "Neutron Diagnosis of Compressed ICF Targets."

M. C. Richardson, G. Pien, P. D. Goldstone, R. H. Day, F. Ameduri, and G. Eden, "Computerized 3-GHz Multichannel Soft X-Ray Diode Spectrometer for High Density Plasma Diagnosis," to be published in *Nuclear Instruments and Methods*.

M. C. Richardson, P. W. McKenty, R. F. Keck, F. J. Marshall, D. M. Roback, C. P. Verdon, R. L. McCrory, and J. M. Soures, "High Aspect-Ratio Laser Fusion Targets Driven by 24 Beam UV Laser Radiation," to be published in *Physical Review Letters*.

M. C. Richardson, U. Feldman, J. F. Seely, C. M. Brown, J. D. Ekberg, W. E. Behring, and J. Reader, "Spectrum and Energy Levels of Br XXV, Br XXIX, Br XXX, and Br XXXI," to be published in the *Journal of the Optical Society of America B*.

Conference Presentations

G. Mourou, "Picosecond and Subpicosecond Characterization of Ultrafast Electronic Components Using the Electro-Optic Sampling Technique," presented at the Workshop on Compound Semiconductor Microwave Materials and Devices '86, San Francisco, CA, February 1986.

G. Mourou, "The Role of Ultrafast Optics in Ultrafast Electronics — the Electro-Optic Sampling Technique," presented at DARPA Advanced Electronic Material/Devices and EHF Monolithic Arrays Review Meeting, San Diego, CA, February 1986.

J. Nees, "Electro-Optic Signal Extraction Techniques," presented at the 1986 IEEE Very Large Scale Integration Test Workshop, Atlantic City, NJ, March 1986.

The following presentations were made at the Topical Conference on High-Temperature Plasma Diagnostics, Hilton Head, SC, March 1986:

P. A. Jaanimagi, L. DaSilva, G. G. Gregory, C. Hestdalen, C. D. Kiikka, R. Kotmel, and M. C. Richardson, "Optical Fiducials for X-Ray Streak Cameras at LLE."

J. S. Wark, A. Hauer, and J. D. Kilkenny, "Studies of X-Ray Switching and Shuttering Techniques."

P. G. Burkhalter, D. A. Newman, D. L. Rosen, K. Hudson, M. C. Richardson, and P. Audebert, "Spectral Measurements from Laser-Produced Plasma in OMEGA."

S. G. Prussin, S. M. Lane, M. C. Richardson, and S. G. Noyes, "Debris Collection from Implosion of Microballoons."

S. M. Lane, M. D. Cable, S. G. Prussin, S. G. Glendinning, D. H. Munro, S. P. Hatchett, K. G. Estabrook, L. J. Suter, M. C. Richardson, P. W. McKenty, D. M. Roback, and C. P. Verdon, "High Yield Direct Drive Experiments at NOVA."

M. C. Richardson, R. Keck, S. A. Letzring, R. L. McCrory, P. McKenty, D. Roback, J. M. Soures, C. P. Verdon, S. M. Lane, and S. Prussin, "Neutron Diagnostics of Compressed ICF Targets."

The following presentations were made at the Fifth Topical Fabrication Specialists Meeting, Las Vegas, NV, March 1986:

R. Q. Gram and H. Kim, "Ablation Layer Coating of Mechanically Non-Supported Inertial Fusion Targets."

H. Kim and J. M. Soures, "Target Fabrication for High Density Target Experiments at the University of Rochester's Laboratory for Laser Energetics."

ACKNOWLEDGMENT

The work described in this volume includes current research at the Laboratory for Laser Energetics, which is supported by Empire State Electric Energy Research Corporation, General Electric Company, New York State Energy Research and Development Authority, Ontario Hydro, Southern California Edison Company, the University of Rochester, and the U.S. Department of Energy Office of Inertial Fusion under agreement No. DE-FC08-85DP40200.